

# A PIV Study of Separated Flow around a 2-D Airfoil at High Angles of Attack in a Low Speed Wind Tunnel

Richard Holm

Jonas Gustavsson





*FLYGTEKNISKA*

*FÖRSÖKSANSTALTEN*

*THE AERONAUTICAL RESEARCH INSTITUTE OF SWEDEN*

*Box 11021, SE-161 11 Bromma, Sweden*

*Phone +46 8 555 490 00, Fax +46 8 25 34*

## Abstract

Wind tunnel tests were carried out in order to acquire experimental data for validation of numerical results from Navier-Stokes calculations (CFD-simulations) on airfoils at high angles of attack. The tests were performed on the 21% thick FFA-W3-211 airfoil geometry, 2-dimensional wind tunnel model with 0.45m chord and 2m span. The purpose of the study was to examine the flow field around the airfoil at 8° and 15° angle of attack, in particular to determine the position of the separation and the recirculating region. The wind tunnel tests were carried out at  $Re=1.25$  million. The used measurement techniques were pressure measurement, oil flow visualisation and PIV (Particle Image Velocimetry)

The boundary layer transition was triggered at a fixed position ( $x/c=0.026$  on the suction side and  $x/c=0.312$  on the pressure side) by means of an adhesive zigzag tape. The uncertainties regarding the position of transition was thereby reduced.

Based on the velocity vector field obtained by the PIV data the velocity profile, boundary layer quantities and the back-flow coefficient were derived. The back-flow coefficient was then used as a criterion for separation.

The conclusions of the study were:

- The flow field was determined by PIV and available for comparison with CFD-results.
- Based on the velocity field the separation position, the velocity profile at different chordwise positions and boundary layer quantities were derived.
- The separation position, for 15° angle of attack, was determined in the PIV measurements to  $x/c=0.39\pm0.03$  and in the pressure measurements to  $x/c=0.40\pm0.05$  and somewhat subjectively in the oil flow to  $x/c\approx0.42$ .

The data are available on file format for comparison with CFD results.



# Table of contents

<b>1</b>	<b>Introduction .....</b>	<b>9</b>
1.1	Purpose .....	10
1.2	Background .....	10
<b>2</b>	<b>Methods .....</b>	<b>13</b>
2.1	The wind tunnel L2000.....	13
2.2	The airfoil model and the wind tunnel set up.....	14
2.3	The transition tape.....	15
2.4	The oil flow visualisation.....	16
2.5	Data acquisition and pressure transducers .....	17
2.6	PIV set up and PIV acquisition system.....	18
2.7	The seeding.....	19
2.8	Validation and analysis of PIV data.....	19
2.8.1	Validation criteria .....	19
2.8.2	Analysis .....	20
2.9	Determination of the separation point position .....	20
2.9.1	Static pressure distribution .....	20
2.9.2	Oil flow visualisation.....	21
2.9.3	PIV.....	21
2.9.3.1	Back-flow coefficient $\chi$ .....	21
2.9.3.2	Shape factor .....	21
2.9.3.3	Wall shear stress .....	22
<b>3</b>	<b>Results .....</b>	<b>23</b>
3.1	Results for 8° angle of attack.....	24
3.1.1	Pressure distribution .....	24
3.1.2	The oil flow visualisation .....	26
3.1.3	PIV results .....	27
3.2	Results for 15° angle of attack.....	27
3.2.1	Pressure distribution .....	28
3.2.2	The oil flow visualisation .....	31
3.2.3	PIV-results at h=0.85 m spanwise position.....	32
3.2.3.1	Boundary layer quantities .....	33
3.2.3.2	Determination of separation point.....	37
3.2.4	Spanwise variations .....	38

3.2.4.1	Oil flow visualisation.....	38
3.2.4.2	PIV measurements .....	40
<b>4</b>	<b><i>Discussion</i> .....</b>	<b>45</b>
<b>4.1</b>	<b>Transition tape height .....</b>	<b>46</b>
4.1.1	Reflection on the estimation of the required trip height .....	46
4.1.2	Tests with a 0.4mm high transition tape and a change to a height of 0.2mm .....	47
4.1.3	Determine the roughness Reynolds number for the 0.2mm tape. ....	47
4.1.4	Expected transition position .....	48
<b>4.2</b>	<b>Error and uncertainties in the pressure measurements.....</b>	<b>54</b>
<b>4.3</b>	<b>Error and uncertainties in the PIV-results .....</b>	<b>55</b>
4.3.1	Scale factor, offset and alignment.....	55
4.3.2	Velocity discretisation and velocity gradients .....	56
4.3.3	Errors due to the post processing of the PIV data.....	58
4.3.3.1	Validation .....	58
4.3.3.2	Smoothing.....	59
4.3.3.3	Extrapolation.....	60
4.3.3.4	Temporal variations .....	62
4.3.4	Determination of the free-stream conditions .....	62
<b>5</b>	<b><i>Conclusions</i>.....</b>	<b>65</b>

## Nomenclature and subscripts

$\alpha$	angle of attack (alfa) [°]
$c$	chord [m]
$\chi$	back-flow coefficient [-]
$c_f$	wall shear stress coefficient, $\tau_w/0.5\rho U_\infty^2$ [-]
$C_p$	pressure coefficient, $(p-p_{0\infty})/0.5 \rho U_\infty^2$ [-]
$C_l$	lift coefficient [-]
$C_d$	drag coefficient [-]
$d$	interrogation area side length [m]
$\delta$	total boundary layer thickness [m]
$\delta^*$	displacement thickness [m]
$h$	identical with $z$
$H, H_{12}$	shape factor, $H=\delta^*/\theta$ [-]
$k$	transition tape thickness [m]
$n$	number of collected samples, number of cells of rotating perturbation flow [-]
$\nu$	kinematic viscosity [ $m^2 s^{-1}$ ]
$p$	static pressure [ $kgm^{-1}s^{-2}$ ]
$Re$	Reynolds number based on chord( $Re=U_\infty c/\nu$ ) [-]
$S$	object-to-image scale factor (m/pixel) [m]
$\theta$	momentum thickness [m]
$\Delta t$	time between the two exposures in a picture pair [s]
$\tau$	shear stress [ $kgm^{-1}s^{-2}$ ]
$U$	mean velocity in the x-direction [ $ms^{-1}$ ]
$u$	instantaneous velocity in the x-direction [ $ms^{-1}$ ]
$\Delta u$	velocity discretisation, maximum deviation from mean velocity in an interrogation area [ $ms^{-1}$ ]
$u'v'$	mean of the product between $u$ and $v$ over time [ $m^2 s^{-2}$ ]
$V$	mean velocity in the y-direction [ $ms^{-1}$ ]
$v$	instantaneous velocity in the y-direction [ $ms^{-1}$ ]
$W$	mean velocity in the z-direction [ $ms^{-1}$ ]
$w$	instantaneous velocity in the z-direction [ $ms^{-1}$ ]
$x$	chordwise coordinate (positive down-stream) [m]
$x_b$	position of the rear paint-accumulation line [m]
$x_s$	position of mean separation [m]
$y$	chord-normal coordinate (positive away from the chord towards the suction side of the airfoil)[m]
$y'$	surface-normal coordinate directed away from the airfoil surface [m]
$z$	spanwise coordinate (positive away from the wind-tunnel floor) [m]

# Subscripts

$\infty$	free stream condition
0	condition after isentropic stagnation
e	condition outside the boundary layer, i.e. $y \geq \delta$
w	wall condition, surface condition
rms	root mean square
s	separation
f	fore
a	aft
'	time fluctuation (in combination with velocity)
//	parallel



# 1 Introduction

A wind turbine blade operates at a wide range of angles of attack. For stall-regulated wind turbines, operation in stall is part of their normal condition. In order to calculate the power and loads on wind turbines it is therefore essential to be able to carry out aerodynamic calculations at separated flow conditions. Many research projects deal with the development of numerical models for separated flow. In order to improve these numerical models and validate the results it is important to compare with experimental data.

Traditionally, wind tunnel data include pressure measurements and either static or dynamic balance measurements on an airfoil, but with the introduction of PIV (Particle Image Velocimetry) it becomes possible to determine the velocity field. The velocity field is particularly interesting in the examination of separated flow. However, the velocity field can be determined by other means e.g. hot-wire anemometers or rake devices but the PIV method is especially promising because of its non-intrusiveness. The principle is that particles (seeding) following the flow field are captured in two consecutive digital images, which then are analysed by signal processing into a discrete velocity vector field.

During the years there have been thorough wind tunnel tests of airfoils and recently also with the aim to validate numerical results and improve the numerical models [1]. In many of the wind tunnel tests the velocity field has not been examined and this is a central point in the numerical calculations. The PIV technique makes it somewhat easier to experimentally determine the velocity field. Recently, a European project was presented [2] where a high-lift two-slotted airfoil model was wind tunnel tested. The purpose was to gain insight into PIV measurements in an industrial wind tunnel environment. The flow field around the 2-D model was examined by PIV, oil flow visualisation and rake devices. The results showed many advantages of the PIV method to conventional methods to examine the flow field. However, when thin boundary layer was to be examined the PIV-result became questionable according to the study. This was due to the resolution and the amount of particles (seeding) in the image.

The PIV method is based on a statistical approach and will always give an average flow field. This has to be concerned. In the referred European project it was not obvious how many samples, which was undertaken to determine the mean velocity field.

Any further analyses of the PIV data (velocity profile, separated region) do not seem to have been carried out in this study.

A central part of PIV measurements is the introduction and choice of the seeding. Olive oil droplets were used as seeding in the referred study [2]. The oil seeding was injected locally by a rake near the honeycomb in the wind tunnel, but they also tested global seeding (recirculation of the particles in the wind tunnel circuit). The PIV data with oil seeding was good but some contamination effects of the oil was reported. Other types of seeding were tested in other studies and seeding with propylene glycol proved to be harmless and suitable for PIV measurements [3]. Recirculating global seeding seems to be favourable, when the facilities admit it, since the impact of the wind tunnel flow is reduced.

## 1.1 Purpose

The purpose of the study was to examine the flow field around the FFA-W3-211 airfoil at 8° and 15° angle of attack. In particular, to determine the separation and the recirculating region foremost at 15° angle of attack. Apart from PIV measurement, pressure measurements and oil flow visualisation was planned within the project.

## 1.2 Background

Since the airfoil model already existed and the wind tunnel L2000 was available the condition was favorable and with the financial support from the Swedish National Energy Administration (STEM) it was possible to carry out wind tunnel tests. The project turned out to be a cooperation between FFA and the Department of Mechanics at the Royal Institute of Technology in Stockholm. This was mainly due to the interest of the PIV technique. The PIV data could then support the ongoing European frame project VISCEL where Navier-Stokes calculations were carried out for this airfoil.

In 1993, tests with the same model at the same wind tunnel L2000 was carried out but under slightly different condition, but with a different purpose [4]. However, some data were useful for comparison. Even if the setup was 2-D, the presumably spanwise variation of the separation line was to be qualitative examined, visualised.

The surface flow pattern may be visualised by tufts or oil flow [5]. Those two methods was compared and showed that tufts was favourable for instantaneous flow motion whereas the oil flow captured the average flow motion [6]. Both methods indicated attached and separated flow well, which is desirable in the present study. The referred study also discussed the impact of the aspect ratio (span/chord) on the spanwise variation, known as stall cells in [6]. With an aspect ratio of 4 they found two cells, stall cells, at  $17^\circ$  angle of attack. Apart from the aspect ratio the variation in separation is presumably also caused by variation of the position of transition (from laminar to turbulent boundary layer). The transition depends on the pressure gradient and hence on the airfoil geometry [7]. Oil flow visualisation can be used to qualitatively indicate the variations, stall cells. In the PIV study [2] oil flow visualisation was applied only in approximately 10 % of span at a midspan region. However, this may hardly show the spanwise variations along the airfoil.

In order to reduce the spanwise variation due to variation of the transition a leading edge roughness can be used [4], [1]. Different kinds of roughness are reported in the literature but a zigzag-shaped adhesive tape is reported to be effective [8]. A fixed transition point is also desirable when comparison with numerical results are undertaken.



## 2 Methods

### 2.1 The wind tunnel L2000

The low speed wind tunnel L2000 is a fan-driven closed circuit wind tunnel. The 5m long test section has a 2x2m cross-section (octahedron) and the contraction ratio is 7.5, see sketch in Figure 1. The speed range is 0-62m/s. In 1985, the turbulence intensity was determined by means of a hot-wire anemometer, see Figure 2 and these measurements were assumed to still be valid as no modifications of the wind tunnel have been carried out since then. The turbulence intensity at 40m/s was found to be 0.15% at the centreline.

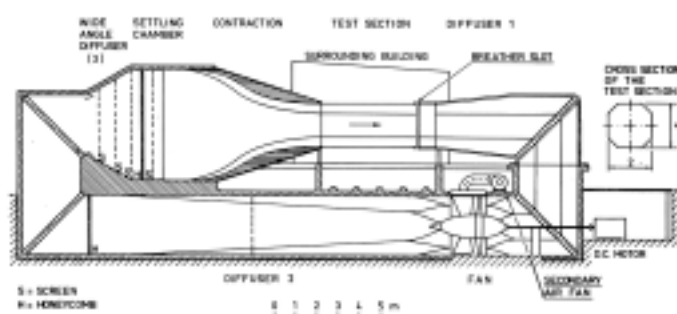


Figure 1: The sketch of the L2000 wind tunnel at the campus of the Royal Institute of Technology (KTH), Stockholm.

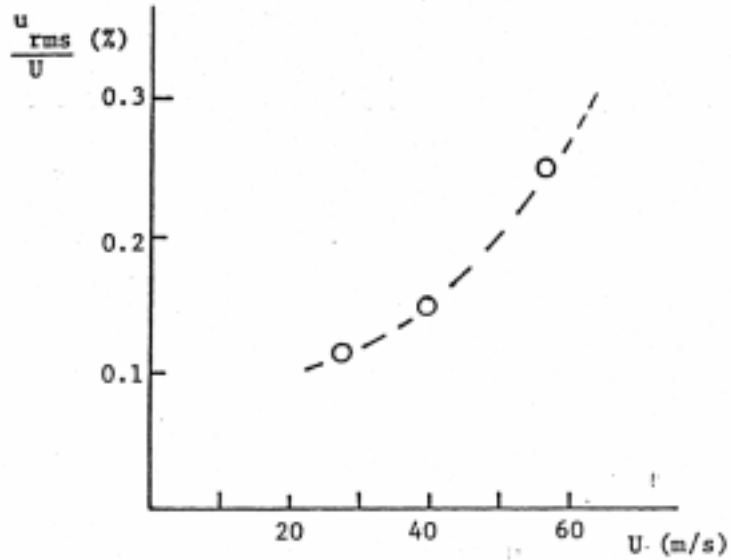


Figure 2: The  $u_{rms}$  measured with a hot-wire anemometer.

## 2.2 The airfoil model and the wind tunnel set up

The model was made of a carbon fibre laminate. It was manufactured and equipped at FFA. The 2-D airfoil model has the geometrical profile, FFA-W3-211. The model has a 2m span, 0.45m chord and 21 % thickness. The model was equipped with 64 static pressure taps, 57 at a chord cross-section situated at midspan, 4 taps at 100mm above midspan and the last 3 taps at 500mm above midspan. The pressure taps off midspan were placed near the leading and trailing edges. The pressure taps in midspan were distributed to measure the pressure distribution in an accurate way.

The model was vertically suspended, 0.13m offset the centre vertical line, to facilitate the use of the PIV system. The lower part of the model was, by means of guidance pins, attached to a turntable. The upper part was a tight beam suspension to a bearing centred on the vertical line. Thus this permitted rotation around the vertical line only and consequently a variation of angle of attack. The angle of attack was determined with an accuracy of  $0.1^\circ$ .

A horizontal plane was examined in the PIV measurements,. In order to acquire the spanwise variations, the plane was placed at five different

vertical positions,  $z=0.85\text{m}$ ,  $0.81\text{m}$ ,  $0.77\text{m}$ ,  $0.60\text{m}$  and  $0.55\text{m}$  from the test section floor. The laser sheet was aligned horizontally and the camera was placed vertically under the turntable. However, due to the limited space under the test section a mirror was used to allow the camera to be mounted horizontally. Because of the low quality of the mirror some losses were noticed. The camera was mounted on a coordinate table to move the image of the camera to different positions along the airfoil. This was due to the size of the image caused by the lens and the chosen area to cover.

## 2.3 The transition tape

Transition tape, trip wires and distributed roughness have been used in many wind tunnel tests in order to provoke transition. One reason can be to simulate real airfoil surface conditions and another reason can be to provoke transition in subscale wind tunnel tests, e.g. eliminate laminar separation bubbles. Transition tape is also used on e.g. gliders to eliminate laminar separation bubbles and thereby reduce drag.

In the present study the aim was to force the transition at a defined position without disturbing the flow more than necessary. This was reported to be attained with a zigzag tape without incurring undue extra drag [8]. The zigzag tape resulted in a fast transition from laminar to turbulent flow with a relatively low thickness (height of the tape) required for the transition to be complete.

We used zigzag tape from Glasfaser Flugzeugbau Hansjörg Streifeneder. The zigzag tape has wedges with an angle of  $60^\circ$  as shown in Figure 3. The transition tape was attached with the upstream end of the tape located at  $x/c=0.026$  on the airfoil suction side and at  $x/c=0.312$  on the pressure side on the airfoil.

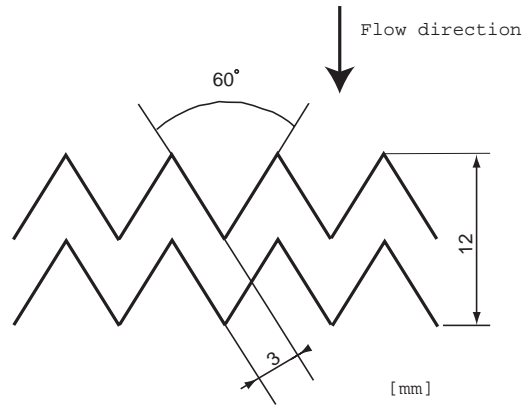


Figure 3: The adhesive zigzag transition tape.

In the first test session (autumn 1998) a nominally tape thickness of 0.4mm was used. During the second session (spring 1999), when the PIV measurements were mainly carried out, the tape thickness was changed to nominally 0.205mm. A discussion on the estimation of sufficient tape thickness to cause immediate transition or not is given in section 4.1.

The actual thickness was measured to be 0.23mm and 0.42mm for the two transition tapes (the tape mounted on a surface).

*Note:* When the 0.2mm tape and 0.4mm is mentioned in the text it refers to the respectively actual thickness (0.23mm and 0.42mm).

## 2.4 The oil flow visualisation

The purpose of the oil flow visualisation was to visualise and quantify the spanwise variations along the airfoil. The average flow pattern was to be examined although some instantaneous motion was noticed. The oil flow or paint, containing a mixture of kerosene and titanium oxide white, was after coating on the airfoil either swept away or remained in different parts on the airfoil surface. Presumably, this was due to the shear stress in the near surface region. The parts with remaining oil flow (paint) were interpreted as regions with low shear stress and thus a separated flow. By using the oil flow visualisation the effect of the adhesive transition tape, its thickness and partly also its position were analysed.



## 2.5 Data acquisition and pressure transducers

One of the fundamental quantities to measure in a wind tunnel test is the pressure, which also was examined in this setup. By means of a Scanivalve (two connection a' 48 taps) the static pressure was measured. Apart from the Scanivalve the pressure acquisition system included five differential pressure transducers (two 0.5 psid and three 2.5 psid from Druck Limited, type PDCR 22), an amplifier FFA Bridge Amplifier (type 1202, insert card type 2341) and a Machintosh II fx with a 12-bit A/D converter card with a voltage range of  $\pm 10$  V. The stagnation pressure was used as reference pressure for the differential pressure transducers. Apart from the airfoil pressure taps the Scanivalve also served the test section wall pressure taps. The wall pressures were measured at four positions (walls, ceiling and floor) in two cross-sections, 2m upstream ( $p_f$ ) and 1.5m downstream ( $p_a$ ) of the airfoil model in the test section. In addition, two airfoil pressure taps were also measured separately (with 2.5 psid transducers) to acquire the fluctuation in time and not only the mean value. The used pressure taps were no.13 or no.17 and no. 20, i.e.  $x/c = 0.54$  or  $0.39$  and  $x/c=0.29$  ( $x/c=1.0$  at trailing edge). Finally, the second 0.5 psid transducer acquired the dynamic pressure.

The calibration of the pressure arrangement was carried out by means of the pressure controller /calibrator Druck DPI 510.

The acquisition program (written in LabView) determined mean, standard deviation, min. and max. for each channel (equivalent to a transducer). The sampling frequency was either 830 Hz during 0.3 seconds or 73 Hz during 10 seconds. The waiting time after the Scanivalve step to start sampling was chosen between 0.1-5.0 seconds. This waiting time was introduced to assure there would be no transient influence on the result.

The wind tunnel quantities, wall pressures and temperature in the test section, were also acquired. Before mounting the airfoil, calibration of the reference dynamic pressure was carried out by a Prandtl tube. The Prandtl tube was mounted at the centreline of the test section. The corrected pressure was assumed to give the dynamic free stream pressure with an accuracy of 2.5 Pa. The temperature transducer, AD 592, has an accuracy of 0.3 K at 298 K according to the product specifications from Analogy Devices.

## 2.6 PIV set up and PIV acquisition system

A two cavity (400mJ each) Nd:YAG laser(Quanta Ray), with a wavelength of 532nm and pulse frequency of 15Hz was used. The duration of the laser beam was 8.0ns. The system belongs to the Department of Mechanics at the Royal Institute of Technology.

Additionally, a digital high-resolution CCD camera (Charge Couple Device), Kodak ES 1.0 was used. The camera either with a 60mm lens or a 105mm lens was able to cover an image of 225x225mm and 90x90mm respectively. The processor and program (FlowMap included FlowManager) used was from DANTEC Measurement technology, Denmark.

Regardless of the geometrical size, the images consisted of 1008x1018 pixels. The images (image pairs) were divided into interrogation areas of 32x32 pixels and with the maximum desirable displacement of 8 pixels of the particles. Combined with an overlap of 25 % of the interrogation areas, the 41x42 velocity vectors were obtained through cross-correlation. The resolution of the field varied from 2.5mm to 5.2mm depending on which camera lens was used.

The average velocity field was based on 150-1300 of the “instantaneous” vector fields. The time between two consecutive vector fields was 0.2-0.6 seconds. The time between the two laser beams, which give the two images of an image pair, was 8 $\mu$ s to 60 $\mu$ s. This time was inspected by a photodiode and an oscilloscope.

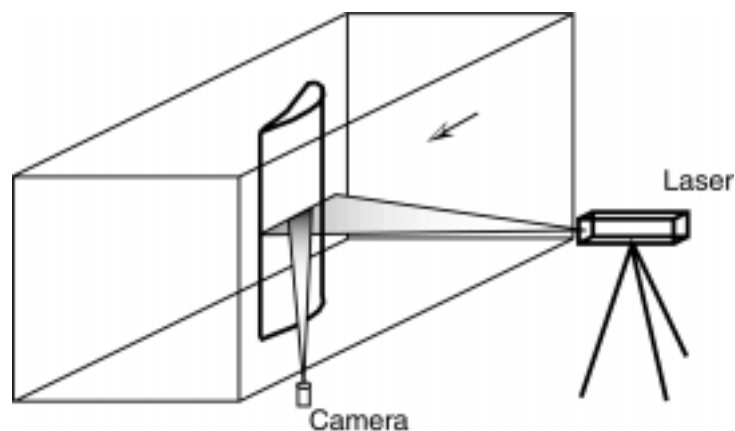


Figure 4: An outline of the PIV setup.

## 2.7 The seeding

Propylene glycol was used as seeding. In the present test the 1,2-Propanediol was diluted with 40 % water and used in the ZR-31 smoke generator (from JEM Smoke Machine Co Ltd, UK). According to [9] the particle size distribution was measured to be 2.0-2.5 $\mu$ m volume median diameter (VMD) and had after 15 minutes been reduced to 1 $\mu$ m (VMD). The propylene glycol particles evaporate with the vapour pressure of 0.26 mbar at 20 °C [3]

The propylene glycol seeding was simply injected into the wind tunnel by a connection in the breather slots just downstream the test section. This proved to be an easy way to introduce seeding during the running mode to allow it to recirculate in the circuit (global seeding). After the injection there was a few minutes waiting time to give good quality smoke (homogeneous seeding) for the PIV measurements. The PIV measurements were carried out for 10-15 minutes, then the procedure was repeated (2-4 times) with the wind tunnel running continuously.

Another seeding based on oil, Odina oil, was also tested but with no further use. The injection procedure differed for the Odina oil, which was introduced through a slit in the airfoil leading edge (local seeding).

## 2.8 Validation and analysis of PIV data

### 2.8.1 Validation criteria

In the process to build up the velocity field the data were validated. The validation means that vectors that did not fulfil certain criteria were considered to be questionable and hence removed. Instead, they were replaced with a fictive vector (more representative than raw data) created in some statistical way, like mean of the surrounding vectors. This is known as hole filling. In the present study, the following validation was used.

- 1) A preliminary calculation of mean and rms velocities was carried out using the validation procedure in the FlowManager program. This validation was a combination of peak validation (Peak Value Ratio > 1.2) and global range validation. The range validation was adjusted to each flow field whereas the peak value was fixed. This resulted in a temporal velocity vector field.

- 2) Based on the temporal mean and rms values, a second validation was carried out using all the raw data once again. Vectors within 3 local rms values of the local mean velocity that also satisfied the peak value ratio criterion were accepted. Thereby the actual variations in the flow field were treated on a local scale instead of on the global range scale used in the first step. The accepted area in velocity space was shaped like an ellipsoid with the length parallel to the x-axis  $6*u_{rms}$  and the width parallel to the y-axis  $6*v_{rms}$  centred about (U,V).

## 2.8.2 Analysis

The mean velocity field (U,V) and fluctuation field ( $u_{rms}, v_{rms}$ ) were determined from the “instantaneous” velocity fields. The back-flow coefficient  $\chi$  was also calculated throughout the studied area.

In addition to hole filling, smoothing was also applied to the accepted mean velocity vectors. The smoothing was applied to remove some of the noise in the form of small, random spatial variations. At every position in the flow field, a weighed average of itself (by 4 times) and the surrounding vectors (by 1 times) replaced the velocity vector.

The resulting mean velocity field was used to determine the velocity profiles (normal out from the airfoil surface) and then derive the displacement thickness ( $\delta^*$ ), the momentum thickness ( $\theta$ ), the shape factor ( $H=\delta^*/\theta$ ) and the free stream velocity outside of the boundary layer ( $U_e$ ).

## 2.9 Determination of the separation point position

In this study the following criterion was used to determine the separation point position in the pressure measurement, the oil flow visualisation and in the PIV data.

### 2.9.1 Static pressure distribution

In the pressure distribution the region of separation was assumed where the distribution indicated a constant pressure plateau. A plateau in the pressure distribution became more obvious as the angle of attack was increased. The separation position was, somewhat subjectively, determined as to where the pressure plateau started.

## 2.9.2 Oil flow visualisation

In the oil flow visualisation the region where the oil flow remained was interpreted as separated flow regions, see section 2.4. The sharp line, between clean airfoil surface and oil flow (paint), was interpreted as the separation point position ( $x_s$ ) (or line).

## 2.9.3 PIV

In order to determine the separation point from the PIV data three quantities was studied: the back-flow coefficient, the shape factor and the wall shear stress. All three based on the measured velocity field.

### 2.9.3.1 Back-flow coefficient $\chi$

The back-flow coefficient,  $\chi$ , was defined as the portion of the “instantaneous” velocity vectors that projected onto the chord point upstream. In the free stream and in zero or negative pressure gradient boundary layers, the back-flow coefficient,  $\chi$ , will remain very close to zero. When there is a strong adverse pressure gradient it will, however, increase and possibly reach 1 in completely separated areas, since the flow is always directed upstream near the airfoil. Mean separation was defined as the position (line) where the back-flow coefficient at the surface was 0.5. Since no measurements were acquired at the surface itself, linear extrapolation from the measured data (two closest measurements a few millimetres above) was carried out to obtain the surface back-flow coefficient  $\chi_w$ . This approach was reasonable as far as the measured back-flow coefficient, used for the extrapolation near the separation, was 0.2–0.3 [10]. If starting off with lower back-flow coefficients at greater distances from the airfoil the result would be an underestimated back-flow coefficient at the airfoil surface.

### 2.9.3.2 Shape factor

The shape factor, defined as the displacement thickness to the momentum thickness,  $H=\delta^*/\theta$ , increases as a boundary layer approaches separation. While the shape factor for a zero-pressure gradient turbulent boundary layer is around 1.3, separation occurs at a much higher  $H$ , probably somewhere in the range of 2.1-4. There is much disagreement in the literature about the existence, universality and value of a critical shape factor. The present study suggested that  $H=3.4\pm0.3$  at separation. Fortunately,  $H$  increased rapidly around separation at high angles of

attack, so a slightly different critical value was not affecting the separation position significantly.

### 2.9.3.3 Wall shear stress

One of the most common definitions of separation is when the wall shear stress has decreased to zero. By means of von Kàrmàn's momentum integral equation,

$$\frac{d\theta}{dx} + \frac{\theta}{U_e} \frac{dU_e}{dx} (H + 2) = \frac{c_f}{2},$$

the wall shear stress was derived.

In PIV measurements, the wall shear stress is not measured directly, but it can be derived from the velocity profiles through application of von Kàrmàn's momentum integral equation above.

However, the PIV data had a rather coarse spatial resolution compared to the boundary layer thickness (approximately 8 measurement points). Furthermore, the results were a bit too noisy to allow accurate derivation in the spanwise direction. This means that there was substantial uncertainty in the determined separation position using this criterion.

### 3 Results

The result of the study included data for 8° and 15° angle of attack at  $Re=1.2$  million. This scoped the three methods: pressure measurement, PIV and oil flow visualisation. The lift and drag coefficient was derived from the pressure measurement. The drag was thus only the pressure drag. No wind tunnel corrections were applied on those data. The uncorrected lift and drag coefficients versus the angle of attack are shown in Figure 5. The results from former tests in 1993 are also presented. However, those pressure measurements were carried out at  $Re=1.7$  million compared to the present study at 1.2 million.

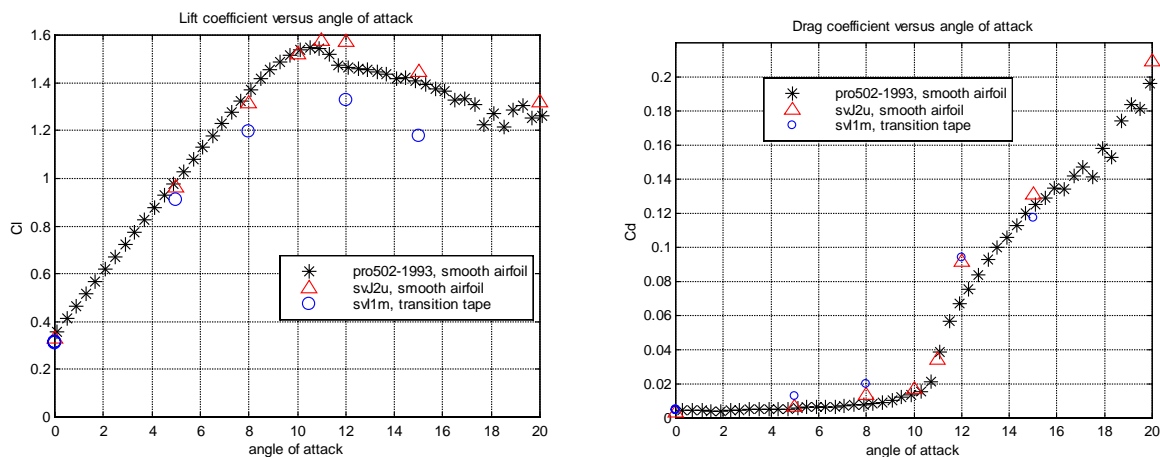


Figure 5: The lift coefficient and drag coefficient derived from the pressure measurement.

The mean velocity field is showed in Figure 6 for 15° angle of attack and summarises data from different chordwise positions. All fields in this figure were obtained by the 105mm camera lens. It shows the outlines of the flow around the airfoil with a separation starting off at approximately half of the chord length. Further downstream a recirculating region can be seen and downstream of the trailing edge some vectors appear with higher magnitude than the surrounding ones. These indicate the flow coming from the pressure side. Since the seeding was global those vectors seems to be reasonable. Further out from the airfoil the free stream field is acquired.

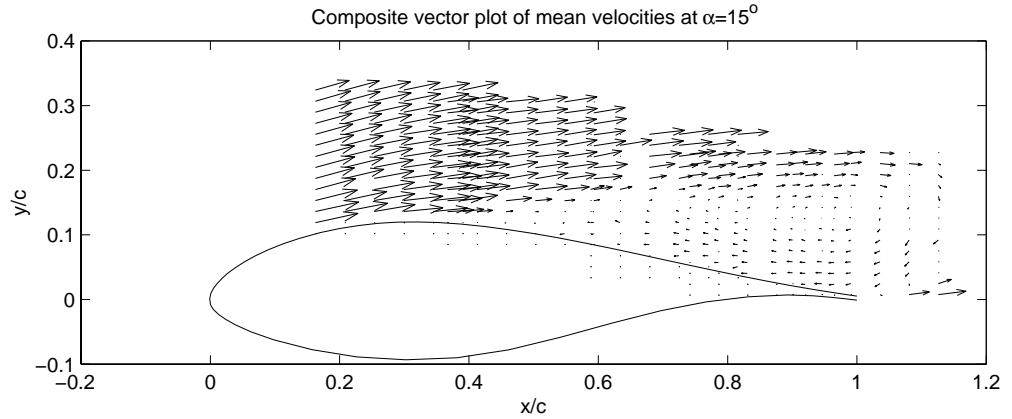


Figure 6: The average velocity field for 15° angle of attack.

### 3.1 Results for 8° angle of attack

This case was selected to represent a case where the flow was essentially attached or with a rather “weak” separation on the airfoil. Thus there would be fairly good chances to determine PIV data as the flow was not so complex as for higher angles of attack.

#### 3.1.1 Pressure distribution

As is mentioned in section 2.9 we were looking for a plateau in the pressure distribution ( $C_p$ ) to find the separation. For the 8° angle of attack case it was difficult to see any plateau towards the trailing edge. Hence it was difficult to locate a separation position as the start of a pressure plateau. Figure 7 shows the pressure distribution ( $C_p$ ) for a case with transition tape compared to a smooth airfoil case. The  $C_p$ -distributions show that the trailing edge velocity is higher for the transition tape case (forced transition). This indicates, to some extent, a separation and a thicker boundary layer. The thicker boundary layer on the suction side near the trailing edge has an effect similar to a negative flap (or de-cambering near the trailing edge) which affects the circulation and the pressure distribution for the whole airfoil. The “pressure plateau”



from the leading edge to  $x/c \approx 0.3$  is therefore at a lower level for the transition tape case.

Notice the peak at the leading edge in the pressure distribution with transition tape, more closely determined to  $x/c=0.039$ . The transition tape had a chordwise extension (12 mm) that covered the pressure tap at  $x/c=0.039$ . A short spanwise “gap” was therefore made in the tape to be able to read this static pressure. However, looking at the peak, the proximity of the transition tape seems to affect the static pressure locally in the region of the tape.

The “jiggles” (discrepancies) in the pressure distribution, e.g. at  $x/c=0.46$  on the pressure side and at  $x/c=0.66$  on the suction side, were due to some strange behaviour of the measured pressures during the test, see section 4.2. For some pressure taps the measured pressure attained values were thought not to be representative for the static pressure. These strange values seemed to appear in an almost random way for one or several taps in many of the test runs. The pressure distributions put into the database should therefore be viewed at with some caution.

For large angles of attack, as will be shown in section 3.2.1, the pressure variation with time was substantial. However, for  $8^\circ$  angle of attack the pressure variation for each tap (min and max) during the measuring time (0.3 s or 10s) was very insignificant and within the resolution of A/D converter ( $\Delta C_p \leq 0.005$ ).

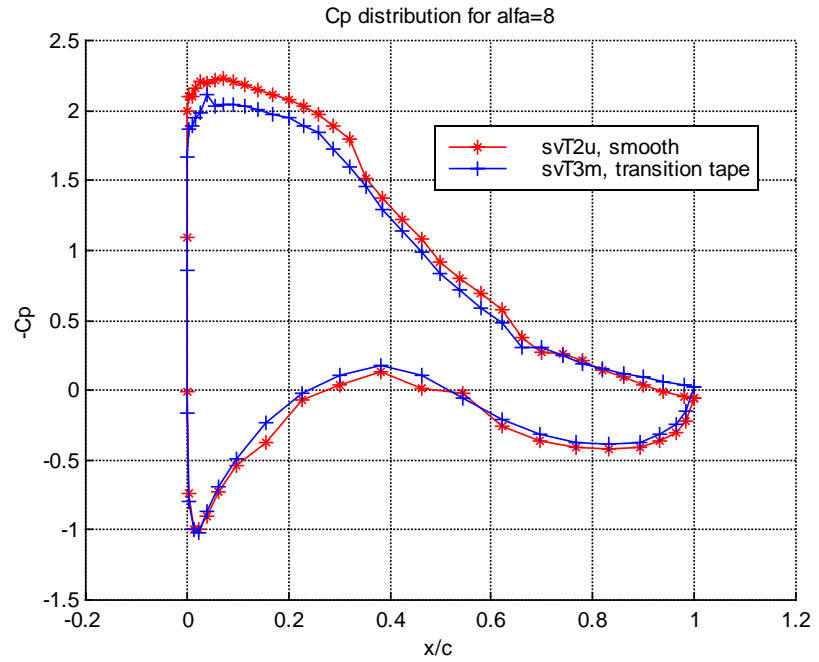


Figure 7: Pressure distribution ( $C_p$ ) for  $8^\circ$  angle of attack for measurements with and without transition tape.

### 3.1.2 The oil flow visualisation

Even if it was hard to see differences between forced transition and smooth airfoil condition in the pressure distribution the oil flow visualisation showed a more significant difference. The oil flow with forced transition indicated a separation at the trailing edge, the right photo in Figure 8, whereas for the smooth airfoil it did not. The location of the separation was approximately determined to  $x/c = 0.8$  and the separation line was fairly straight in the spanwise direction. In the left photo, which shows the result for the smooth airfoil, a laminar bubble at  $x/c = 0.34$  can be seen. It indicates the free transition region from laminar to turbulent boundary layer. The white streaks are just an effect of the gravitational influence on the paint.

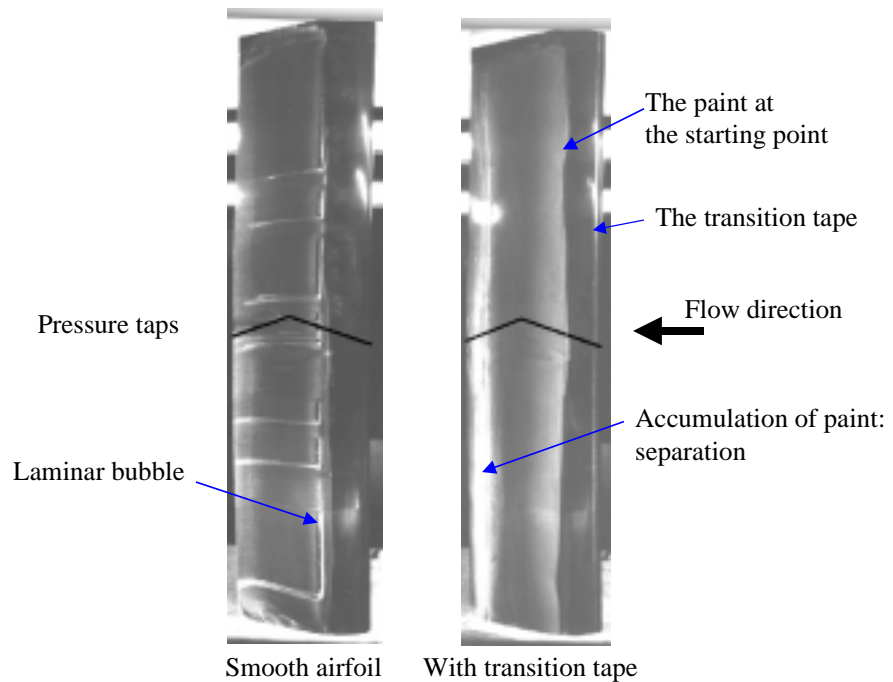


Figure 8: The oil flow visualisation for  $8^\circ$  angle of attack. The photo to the left shows a smooth airfoil and the one to the right with transition tape mounted at the leading edge.

### 3.1.3 PIV results

A few PIV measurements were carried out at  $8^\circ$  angle of attack only at interesting chordwise positions, such as the indicated region of separation in the oil flow tests. The result of the PIV data indicated separated flow in the region  $x/c > 0.85$ . This separation was very ‘weak’ in the sense that the boundary layer growth was moderate. The shape factor ( $H$ ) remained in the range 3.9-4.1 for all chordwise positions over the studied image region (J3,  $x/c = 0.85$ -1.02). Low quality measurements (B1, C1) further upstream suggested separation not too far away from  $x/c = 0.8$  (say  $\pm 5\%$ ). Those measurements were carried out as first trials in the beginning and with the 60mm lens i.e. a big area but with poor resolution when the separation point is to be determined.

## 3.2 Results for $15^\circ$ angle of attack

The present study focused on  $15^\circ$  angle of attack, mainly because of the fact that Navier-Stokes calculation was carried out at this angle of attack. At  $15^\circ$  angle of attack the flow was suspected to have reached a significant separation with a much more obvious recirculation region.

The flow field would be more complex than for 8° angle of attack but of more interest if separated flow was to be examined.

### 3.2.1 Pressure distribution

For 15° angle of attack the pressure distribution ( $C_p$ ) showed a sharp pressure peak and a more obvious pressure plateau than at 8° angle of attack. The constant pressure plateau in Figure 9 was interpreted as a separated flow region. The separation point position was determined to  $x/c=0.38 \pm 0.03$ . The max and min variations are also presented in Figure 9. The max and min variations may be up to 25%, during the acquisition time, in the foremost region from the leading edge to the pressure plateau, whereas the variations in the region of constant pressure and on the pressure side were less. The off midspan pressure coefficients (0.1 and 0.5m off midspan) are also presented. They all agree well with the midspan distribution. All the pressure data in Figure 9 were 10s average (73Hz). Max and min correspond to the extreme values during this 10s acquisition time.

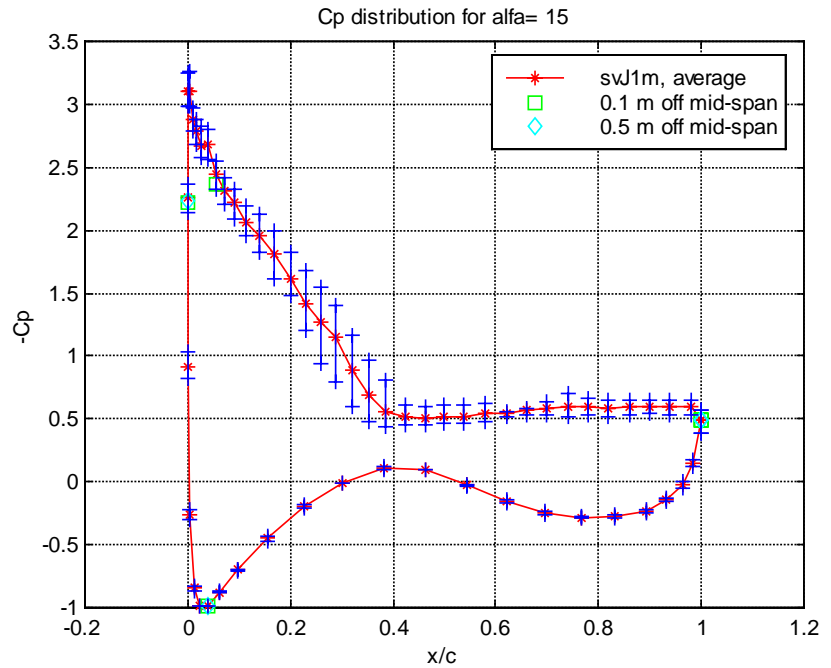


Figure 9: The pressure distribution, average, min and max and also the off midspan pressure coefficient.

The pressure distribution ( $C_p$ ) versus time measured for at the two chordwise positions on the suction side,  $x/c=0.387$  and  $0.289$  are shown

in Figure 10. The figure shows the average, min and max  $C_p$  acquired during 10 s and 73 Hz for each time-step. This shows the variation of the mean value for every acquisition time (10 s). The variation of the max and min were on a fairly constant level from one acquisition time to another, which showed that even if there was an unsteady flow structure the mean  $C_p$  showed some representative average value. The range (min-max) at  $x/c=0.387$  are less than at  $x/c=0.289$ . This is also seen in Figure 9 where the range (min-max) is wider in the region with strongly adverse pressure gradient than other regions (looking on the suction side).

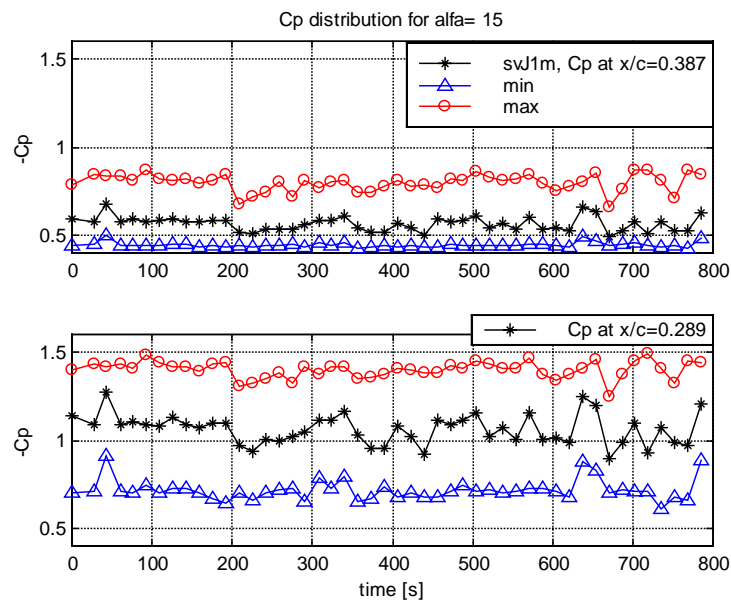


Figure 10: Average, min and max pressure coefficient ( $C_p$ ) at  $x/c=0.387$  and 0.289.

Three representative pressure distributions for a *smooth* airfoil are shown in Figure 11. The acquisition time in the first run was 10 sec. whereas in the second and the third, the acquisition time was 0.3 sec. This shows a reproduction and consistency in the pressure measurements, both regarding different tests and different experimental setup. The third one (sv983u) was acquired in the autumn session. The separation for a smooth airfoil was determine to  $x/c= 0.50 \pm 0.02$ . The “jiggles “ (discrepancies) at  $x/c=0.48$  on the pressure side was assumed to be due to the imperfection of the pressure measurements.

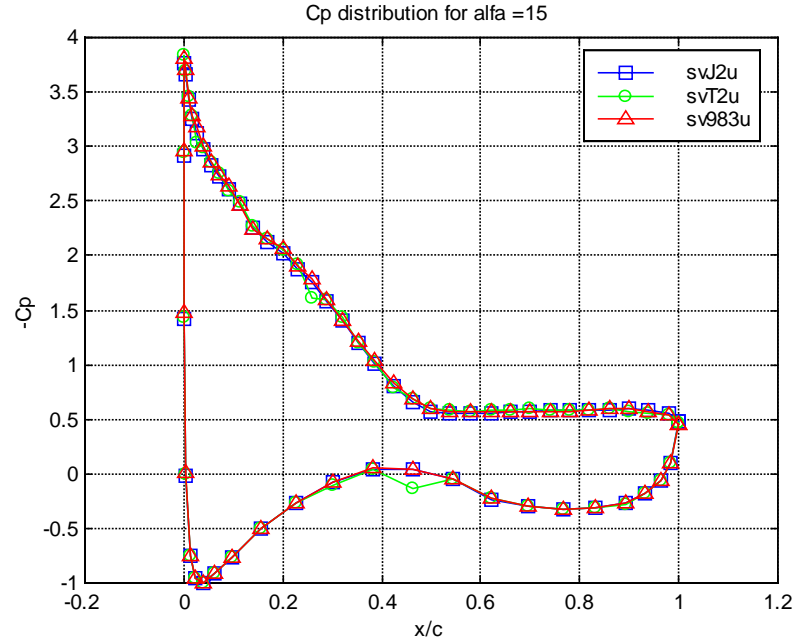


Figure 11: The pressure distribution for three representative measurements for smooth airfoil.

The  $C_p$  variation in time for  $x/c=0.289$  for a smooth airfoil, is shown in Figure 12. There are two runs with different acquisition time (0.3s and 10s). The mean, min and max values are presented for each time-step. During the 10s acquisition time (lower part of Figure 12) the max and min values were constant, apart from some occasional jiggles during the first points, whereas the shorter acquisition time (0.3s) shows some variations of max and min. This could indicate some pressure variations longer than 0.3s, but less than 10s and they may be caused by shifts in the flow field structure, e.g. a moving separation position. This may have caused the dip after 58s in the upper part of Figure 12. However, the mean  $C_p$  is of the same order for both runs and the uncertainties in the mean  $C_p$  is within the range of min and max values for the 10s acquisition time. This is interpreted as the mean  $C_p$  was assumed to be a time independent mean value. When comparing the same chordwise position ( $x/c=0.289$ ) for an airfoil with transition tape and smooth airfoil the variations of mean  $C_p$  are significantly higher for the transition tape case. The tape seems not only to provoke transition but also to add some fluctuations. These fluctuations influenced the pressure variation at this tap and the same was also observed for the chordwise position  $x/c=0.387$ .

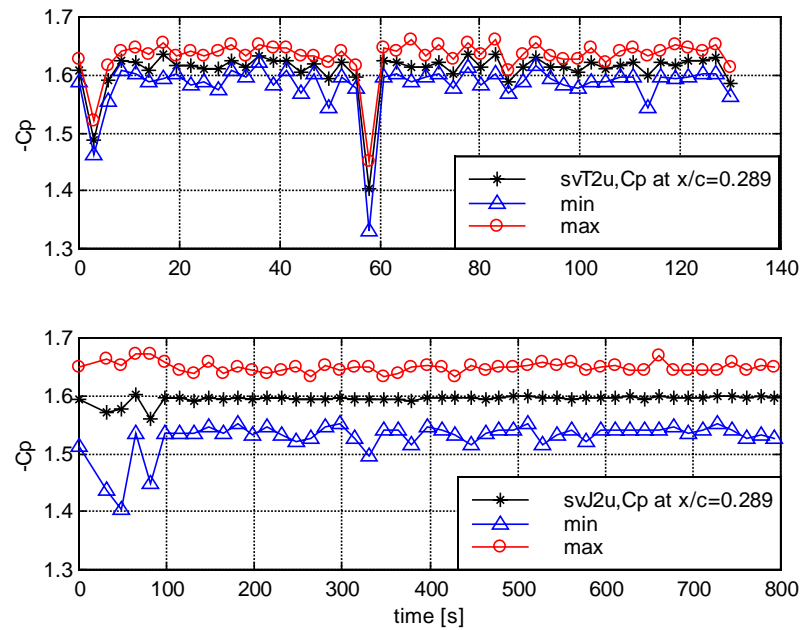


Figure 12: The  $C_p$  variation in time for two different acquisition time, average of samples during 0.3 sec.(830 Hz) and 10 sec (73 Hz). Both pressure measurements for smooth airfoil case.

### 3.2.2 The oil flow visualisation

The oil flow visualisations for  $15^\circ$  angle of attack showed a significant difference with or without transition tape, see Figure 13. Examination of the photos indicated separation at  $x/c \approx 0.4$  at  $h=0.85$  m for the case with transition tape. However, it should again be pointed out that the main purpose of the oil flow tests was to give insight into the flow pattern on the airfoil surface rather than to quantify the position of separation. A discussion of the spanwise variation and estimates of the separation position at different spanwise positions is given in section 3.2.4.1.

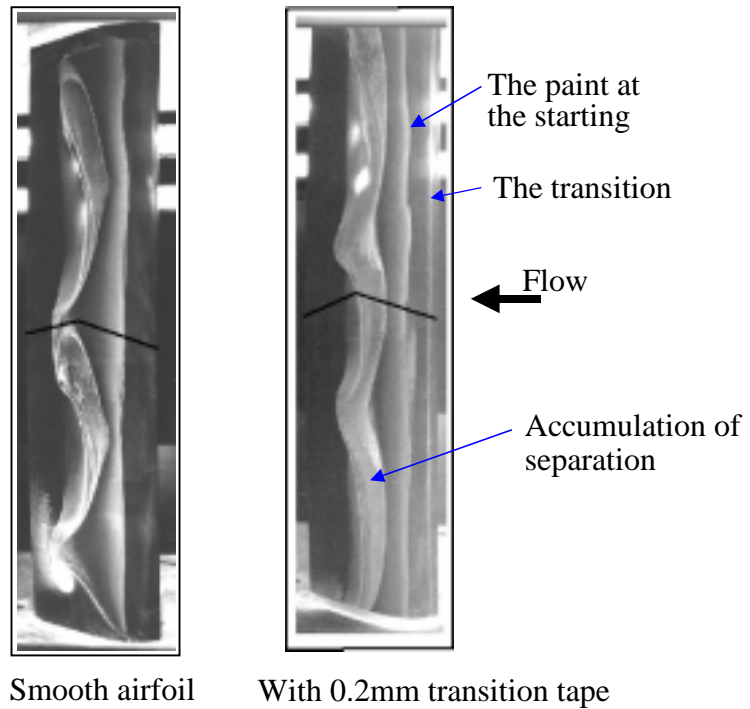


Figure 13: The oil flow visualisation for 15° angle of attack.

### 3.2.3 PIV-results at $h=0.85$ m spanwise position

The following image areas were used for the PIV measurements, see Figure 14. A 105mm lens was used to obtain those image areas except for A1 and C4 where a 60mm lens was used. The reference point is the lower left corner in all images.

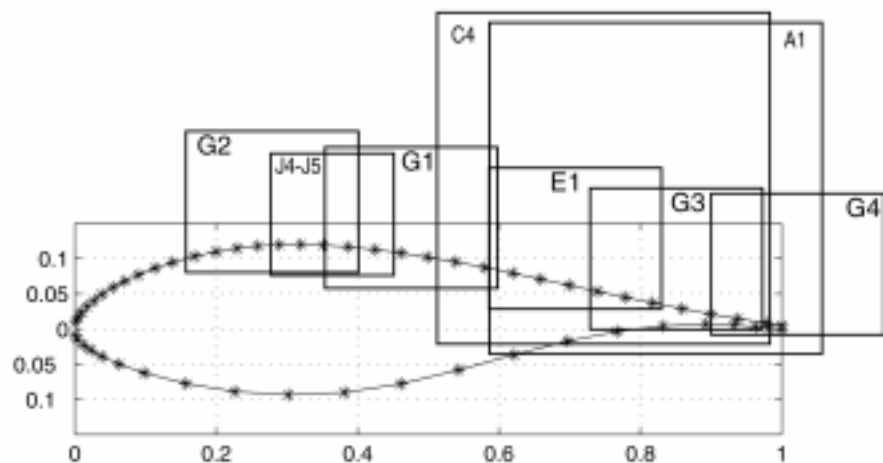


Figure 14: The image areas for the PIV measurements at 15° angle of attack. The reference point was the lower left corner in the image corresponding to the image position in Table 13 in Appendix 1.



### 3.2.3.1 Boundary layer quantities

The boundary layer quantities derived from the PIV measurements are presented in Table 1. As the examined areas in some cases have an overlap a direct comparison was possible. The quantities were derived at some arbitrarily chosen chordwise position ( $x/c$ ).

Table 1: The displacement thickness, momentum loss thickness and shape factor at some arbitrarily chosen chordwise positions.

run:	G2	G2	J4	J4	G1	J4	G1	G1
$x(\text{mm})$ :	119.2	160.2	159.2	180.9	180.4	189.9	190.6	200.7
$x/c$	0.265	0.356	0.354	0.402	0.401	0.422	0.424	0.446
$\delta^*(\text{mm})$ :	2.74	4.76	4.10	8.77	9.00	10.7	11.5	15.1
$\theta(\text{mm})$ :	0.97	1.57	1.27	1.71	2.40	2.15	2.45	2.39
H:	2.83	3.04	3.21	5.12	3.76	4.98	4.70	6.32
$\delta(\text{mm})$ :	7	12	11	17	20	20	22	25
$U_e(\text{m/s})$ :	54.7	50.1	50.4	48.5	45.0	48.1	43.8	43.3
run:	G1	G1	E1	A1	C4	E1	C4	C4
$x(\text{mm})$ :	221.1	238.9	280.0	318.4	319.6	320.9	361.3	397.8
$x/c$	0.491	0.531	0.622	0.708	0.710	0.713	0.803	0.884
$\delta^*(\text{mm})$ :	22.0	28.4	53.2	61.7	58.3	67.4	74.2	85.8
$\theta(\text{mm})$ :	2.96	3.54	3.26	4.41	2.15	2.92	3.43	4.89
H:	7.45	8.04	16.3	14.0	27.1	23.1	21.6	17.5
$\delta(\text{mm})$ :	33	43	75	90	80	90	105	130
$U_e(\text{m/s})$ :	43.9	44.6	45.5	46.8	45.2	45.1	46.3	46.1

As separation was approached, the displacement thickness ( $\delta^*$ ) started to grow rapidly, see Figure 15 at approximately  $x/c \approx 0.4$ , and this continued in the downstream separated region. Meanwhile, the momentum loss thickness ( $\theta$ ) grew less rapidly than the displacement. In the present study the free stream was not reached within the image area at the most downstream positions when the 105mm lens was used, so this development could not be followed in great detail.

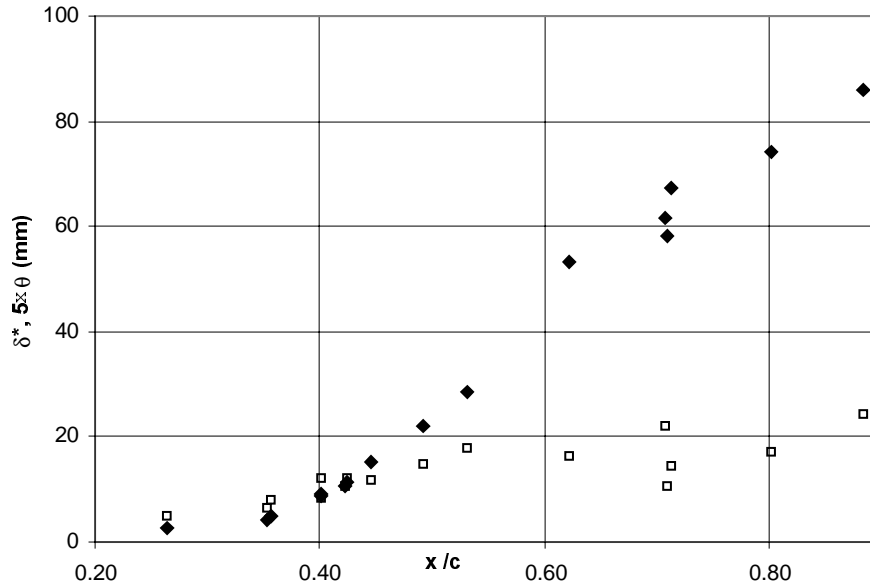


Figure 15. The displacement and momentum loss thickness from PIV measurement at different chordwise position in the chordwise region of the separation position.

As is seen at certain positions, most notably at  $x/c=0.7$  in Figure 15, it was not easy to concatenate measurements carried out at different occasions with one another near the edges of the pictures where they overlap each other. At  $x/c=0.7$ , the difference in  $\delta^*$  between different runs is as large as 10 mm. Figure 16 illustrates this problem through a comparison of the velocity profiles at  $x/c=0.424$  ( $x=191$  mm) and  $x/c=0.422$  ( $x=190$  mm) obtained in run G1 and J4, respectively. As can be seen, the differences are significant, both when it comes to the boundary layer structure and in the velocity outside boundary layer ( $U_e$ ). This may indicate that there are considerable differences in the flow field around the profile measured at different occasions. The last row of Table1 suggests that the velocities obtained during run G1, for some reason, are about 10 % too low. This is also illustrated in Figure 16.

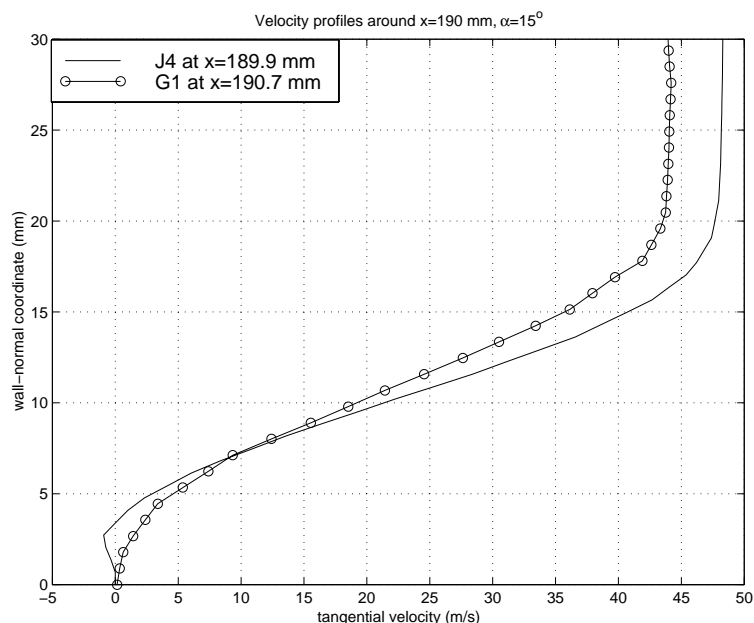


Figure 16. The velocity profile normal to the airfoil surface in the overlapping region for the two cases J4 and G1 at  $x/c=0.422$ .

Another comparison was made near  $x/c=0.356$  ( $x=160$  mm), where the runs G2 and J4 overlapped. The velocity profiles obtained are found in the Figure 17. As can be seen, even though the velocities outside the boundary layer are very similar, there is a significant difference in the shape of the velocity profile and thus in the thickness of the boundary layer. It seems that there was some kind of variation either in the flow or in the measurement setup between the two runs.

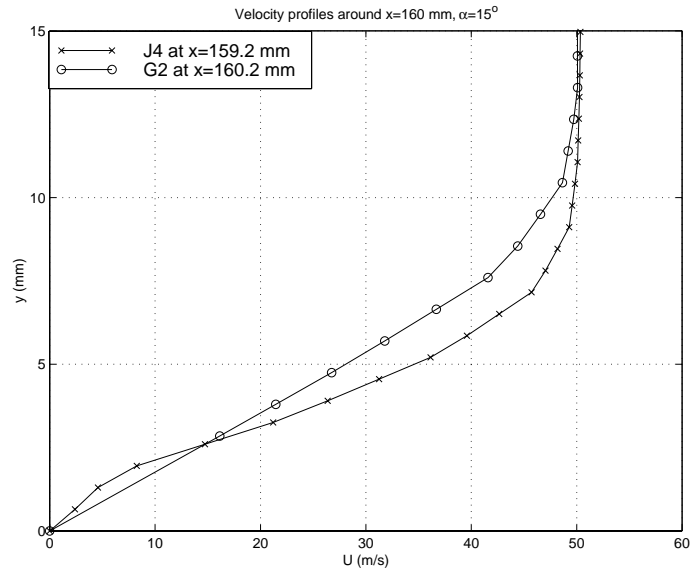


Figure 17. The velocity profile normal to the airfoil surface for another chordwise position ( $x/c=0.356$ ) compared to Figure 16.

Figure 18 demonstrates how the displacement thickness at  $x/c=0.444$  ( $x=200$  mm) depended on the separation position. Early separation correlates with a thick boundary layer at this position. This could be interpreted in two ways:

- There were differences in the boundary layer thickness even upstream of the separation position and a thick boundary layer (which has a low skin friction) separated more easily than thinner boundary layers.
- A separated boundary layer grew more rapidly than an attached layer.

In reality, the trend the Figure 18 was believed to be a result of a combination of these effects, where the differences in separation position accentuate the thickness differences in the spanwise position even existing prior to separation.

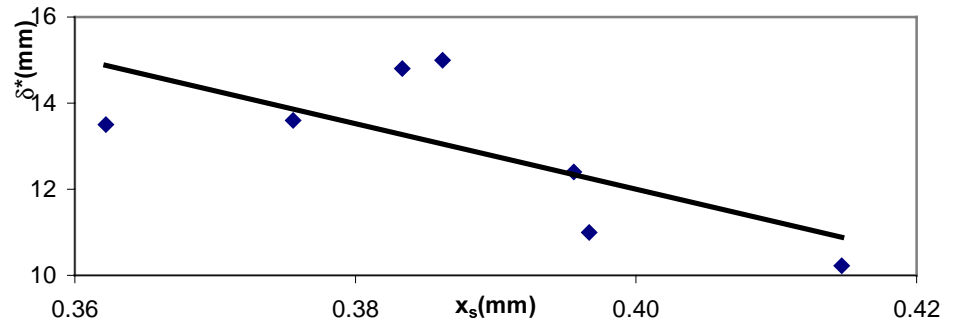


Figure 18. The variation of displacement thickness at some chordwise positions in the region of the separation position

### 3.2.3.2 Determination of separation point

The position of mean separation can be found using several different methods. In this report, the separation position has mainly been defined as the position where the back-flow coefficient at the surface was 50% or more, see section 2.9.3. To check the sensitivity of this approach, two other methods have been tested below, the shape factor criteria  $H=3.4$  and zero skin friction ( $c_f \leq 0$ ) at separation position.

#### Determination by back-flow coefficient $\geq 0.5$

Three different measurements were made around separation (J4, J5 and G1). The composite result of these measurements, suggests separation ( $\chi_w=0.5$ ) at  $x/c=0.372 \pm 0.014$ , where the shape factor was derived to  $H=3.4 \pm 0.3$ .

#### Determination by shape factor, $H \geq 3.4$

Using shape factor  $H=3.4$  as a separation criterion in the three measurements that were made around separation resulted in a separation point position of  $x/c=0.377 \pm 0.006$ .

#### Determination by skin friction coefficient, $c_f \leq 0$

The boundary layer parameters were calculated from the velocity profiles near separation. By using von Kàrmàn's integral equation the skin-friction coefficient  $c_f$  was derived. The  $c_f$  was found to reach zero at  $x/c=0.372$ .

## 3.2.4 Spanwise variations

### 3.2.4.1 Oil flow visualisation

Oil flow visualisation was used as a qualitative method to visualise the spanwise variations. At  $8^\circ$  angle of attack (Figure 8) the photos show only insignificant spanwise variation of the separation line.

However, for  $15^\circ$  angle of attack the variations were substantial, especially for the smooth airfoil. The cause for such spanwise variations, and the occurrence of stall cells<sup>1</sup> is not fully understood but recently reported by Yon and Katz [6].

Figure 13 shows that the inclusion of the transition tape significantly reduced the spanwise variations of the separation line. The tested airfoil, and other thick airfoils, is very sensitive to leading edge roughness. With transition moved upstream of the free transition position, the boundary layer downstream will be thicker than it would be with free transition, and the separation will move upstream. Some of the larger spanwise variations for the smooth airfoil case could be caused by the transition being at different chordwise positions transition, resulting in different position of separation and this phenomenon locking itself in the spanwise direction.

By varying the aspect ratio Yon and Katz [6] found a relation between the aspect ratio and the number of stall cells on the airfoil. For the smooth airfoil case in the current study the oil flow visualisation in Figure 13 shows essentially two stall cells. With the aspect ratio of 4.4 this agrees well with what was observed in [6]. On the other hand, for the transition tape case the number of stall cells could be interpreted as three.

Figure 19 below shows that there is a difference between the cases with the 0.2mm and 0.4mm transition tape with less spanwise variation for the thicker tape. The separation position derived from an analysis of the oil flow visualisation is further upstream for the 0.4mm transition tape case. Note that this is contrary to results obtained by looking at pressure distributions, where the separation position, defined as the start of the pressure plateau, in general seems to be slightly further upstream for the 0.2mm tape case.

---

<sup>1</sup> stall cells as defined in [6] as cells where the separation has moved upstream, surrounded by more attached flow.

It should also be remarked that Figures 12 and Figure 19 only show samples of oil flow visualisations. The three cell “seagull “ wing pattern repeated itself for three visualisations with the 0.2mm tape mounted on both the sides of the airfoil. However, for another visualisation with the 0.2mm tape only on the suction side, only two cells appeared with the separation line at midspan being in an downstream position, contrary to Figures 12 and Figure 19 where the separation line is at a upstream position at midspan. It is questionable if this missing tape on the pressure side could affect the whole flow picture. It could as well be a different flow pattern that occurs for some other reason e.g. the amount of paint even if this tried to be fixed. However, once one pattern (flow situation) had been established it remained until the oil had been swept away “blown away” or dried (time scale of minutes).

Figure 19 below shows the separation line as interpreted from the oil-flow test and Table 2 shows the results from the determination of the separation point position at the different spanwise laser sheet positions where the PIV measurements were taken.

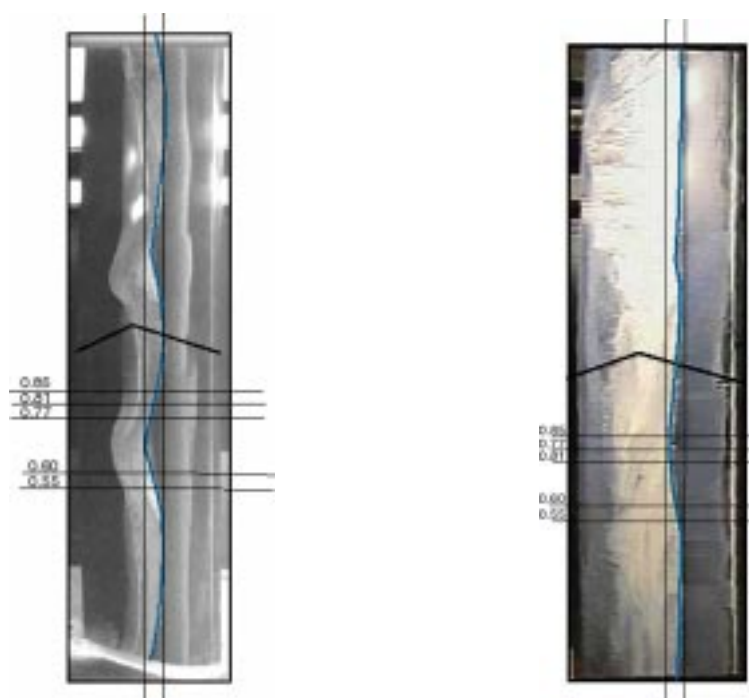


Figure 19: The spanwise variation at 15° angle of attack. The left photo for 0.2mm transition tape and the right photo 0.4mm tape. The two vertical lines show the range of the spanwise variation.

The indicated separation position ( $x_s$ ) and the position ( $x_a$ ) of the equally sharp aft end of the oil flow visualisation are included in Table 2.

Table 2 shows that the separation position is indicated as being further upstream for the 0.4mm tape than 0.2mm. With the 0.4mm tape the separation position was at  $x/c = 0.37 \pm 0.04.2$  and for the 0.2mm tape the position was found to be  $x/c = 0.424 \pm 0.06$ .

Table 2. Spanwise variation of the separation position

h(m)	$x_s/c(\%)$	$x_s/c(\%)$	$x_a/c(\%)$
	0.2mm tape	0.4mm tape	0.2mm tape
0.55	40.6	32.8	68.2
0.60	44.4	32.8	64.2
0.77	45.5	38.1	59.0
0.81	41.7	40.2	56.1
0.85	39.8	40.2	55.2

As mentioned above, the photos in Figure 19 are only samples of oil flow visualisations. However, they fairly well show the amplitude of the observed spanwise variation of the separation position.

#### 3.2.4.2 PIV measurements

The spanwise variations are also seen in the analysis of the PIV data. As Figure 20 shows, the back-flow coefficient varied not only in the chordwise direction, but also between measurements made at different spanwise positions.



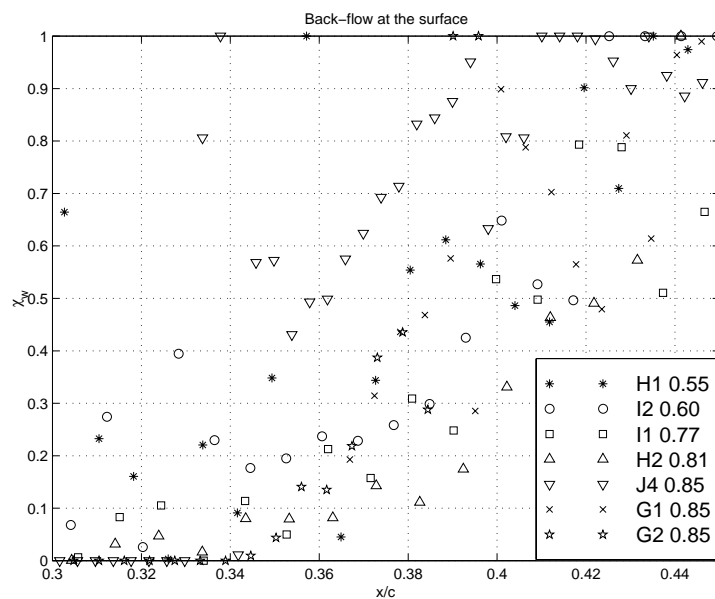


Figure 20: The back-flow coefficient for different chordwise positions, but also for different spanwise positions in the region of separation position for  $15^\circ$  angle of attack.

Figure 20 has been used to find the separation positions where  $\chi_w=0.5$  at five different spanwise positions. The orientation of the images is shown in the Figures 20-22, for the different spanwise positions.

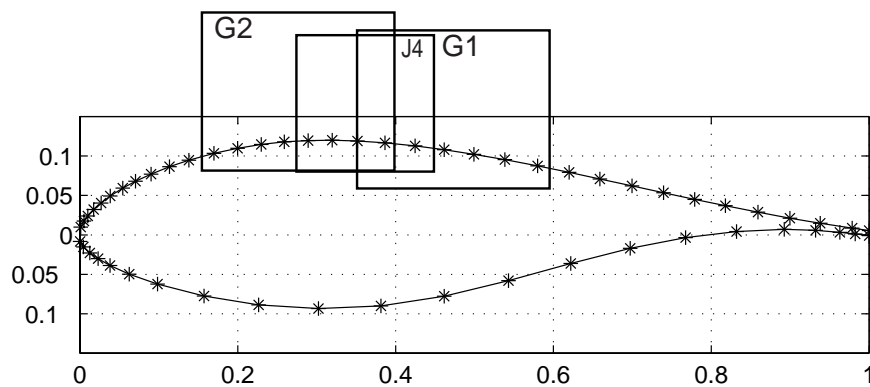


Figure 21: A sketch over the image areas. All with 105 mm camera lens and at 0.85 m spanwise position.

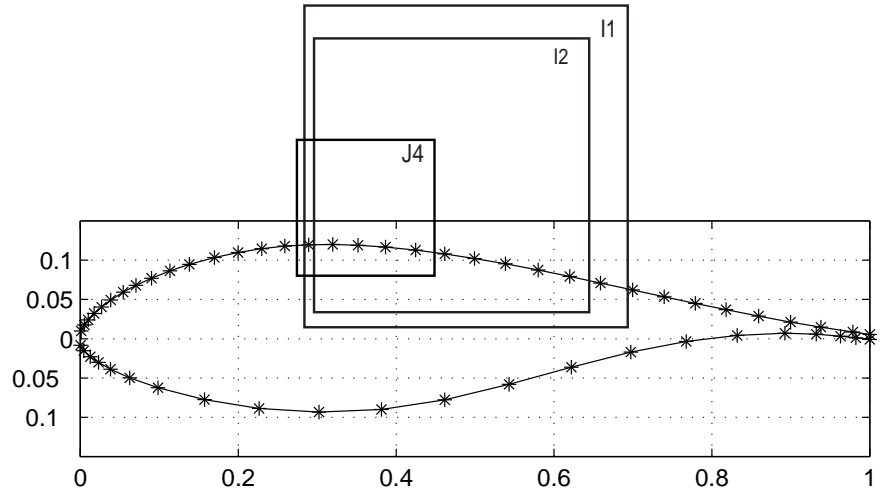


Figure 22: The images with the 60 mm camera lens. I1 at 0.77 m and I2 at 0.60m spanwise position from the test section floor. J4 at 0.85 m and with the 105mm lens.

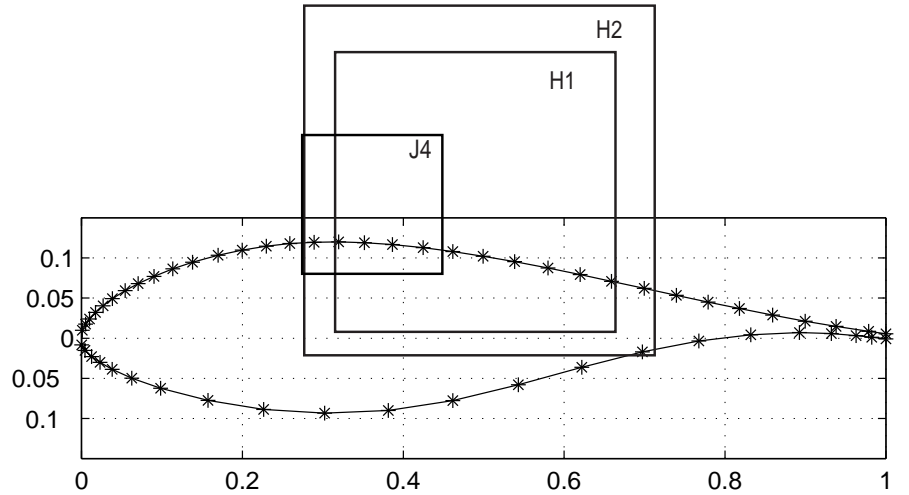


Figure 23: H1 at 0.55 m and H2 at 0.81 m spanwise position. Both with the 60mm camera lens.

The results are given in Table 3, where the separation position and the shape factor are presented for the different spanwise position. A variation in the separation position can be noticed. There are also some variations at the same spanwise position (0.85 m). This was taken into consideration in the analysis of the result at 0.85 m. The shape factor derived at 0.55 m should be taken with some caution as the data was questionable in this case near the separation position.

Table 3. The variation of separation position and shape factor for different spanwise positions.

h(m)	run	x/c	H
0.55	H1	0.376	(2.9)
0.60	I2	0.396	3.8
0.77	I1	0.397	3.5
0.81	H2	0.415	3.4
0.85	J4	0.359	3.1
0.85	G1	0.383	3.5

While the PIV measurements also indicated some spanwise variation, it seemed both different and weaker than the variations found in the oil flow visualisation. To further examine the structure of the flow in the PIV case, the spanwise differential of the spanwise velocity,  $\partial w/\partial z$ , was calculated. This was obtained by applying the continuity equation on the PIV data. In Figure 24, the differentials at a chordwise position and chord normal position ( $x/c=0.6$  and  $y/c=0.122$ ) are shown. All spanwise positions are presented for comparison, but the data from H1 (0.55 m) were excluded.

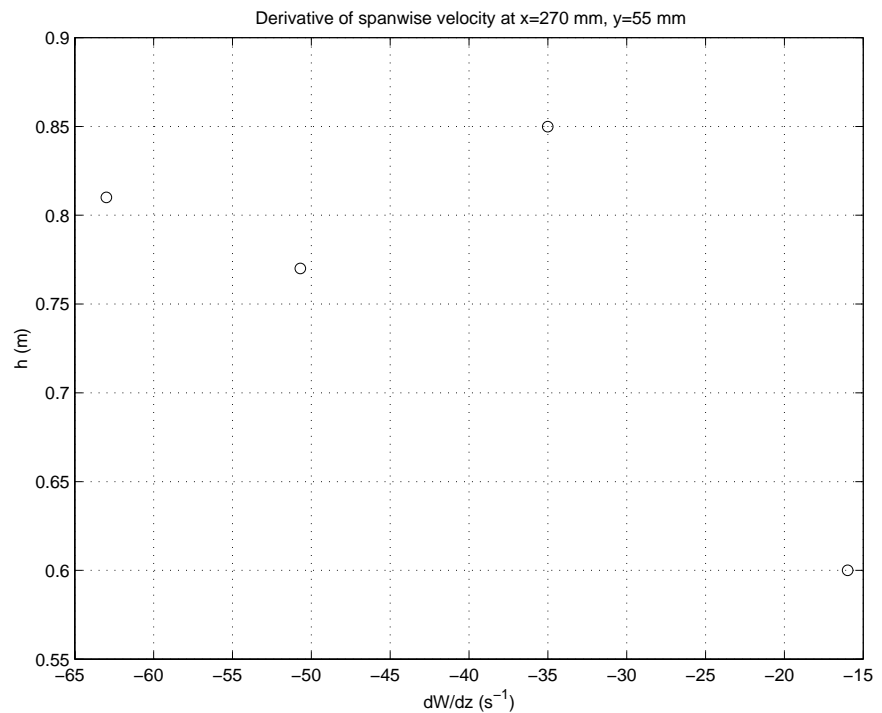


Figure 24. The differential spanwise velocity ( $\partial w/\partial z$ ) at different spanwise positions.

In case the mean velocity perturbations from 2D flow can be described by ellipsoids, the spanwise velocity near the centre of the airfoil span could presumably be described by

$$w(z) = -A \sin\left(\frac{z - z_0}{h} n\pi\right) \quad \frac{\partial w}{\partial z} = -A \frac{n\pi}{h} \cos\left(\frac{z - z_0}{h} n\pi\right),$$

where  $z_0$  is the distance from the floor to the centre of the profile,  $h$  the wind-tunnel height and  $n$  is the number of vortices with rotating mean velocity perturbation flow. As in the oil flow visualisation tests, the number of vortices, excluding the flow that takes place close to the test section floor and ceiling, appeared to be 4 for smooth airfoil (6 vortices with transition tape). Figure 24 indicates that the maximum spanwise differential is in the order of  $80 \text{ s}^{-1}$ . Based on this and the number of vortices, the maximum spanwise velocity seems to be in the order of 10-15 m/s at this (x,y)-position. This is a significant velocity compared to the  $U$  and  $V$  velocities at this position and large enough to affect PIV measurements, where out-of-plane vectors are lost. If high  $W$  velocities in any way correlate with high  $U$  or  $V$  velocities, a bias in the mean velocities in the plane will be the result.

## 4 Discussion

This section includes the discussions of the effect of the transition tape and the uncertainties in the pressure measurements and PIV measurements and some comments on the errors. The uncertainties in the PIV measurement are divided into errors due to physical errors (length, time, etc.) and uncertainties due to the post processing of the PIV data.

Regarding the PIV-method the procedure with the seeding was briefly examined. During the first test session (autumn 1998) local seeding was tested. Seeding (Odina oil droplets) was introduced through a slit at the leading edge (at  $x/c=0.05$ ). The inside of the airfoil model was acting as a chamber for the seeding with the surrounding wind tunnel hall pressure. The procedure was examined by oil flow visualisation, which showed that the open slit influenced the flow pattern remarkably. The separation line moved upstream in the region of the open slit compared to closed slit. This was likely caused by a local mass flux (air transport) through the slit into the boundary layer due to the pressure difference inside the model and on the airfoil surface. The thicker boundary layer then caused an earlier separation.

Neither the PIV result nor the oil flow visualisation result showed any advantages of this test setup hence the global seeding was used during the second test session (spring 1999)

The seeding quantity is however more for global seeding than for local seeding. Visual inspection of the wind tunnel was carried out during the tests and some observations of the propylene glycol right after the use was made. But since propylene glycol evaporates, no cleaning action was carried out.

## 4.1 Transition tape height

As will be discussed below, the tape thickness used in the current test was rather small and this needs some comments. The conclusion, however, is that it was sufficiently high to force transition.

### 4.1.1 Reflection on the estimation of the required trip height

Several rules to estimate the critical height (thickness) of trips and roughness elements exists and the influence of the roughness trips upon boundary layer transition has been reported e.g. by Gibbings, Goksel and Hall [12], [13], [14]. Knowledge is also summarised by Poll [15].

An often-used criterion for critical roughness thickness is the roughness Reynolds number  $R_k$

$$R_k = \frac{k \cdot U_k}{\nu},$$

where  $k$  is the height of the roughness element and  $U_k$  is the velocity in the undisturbed boundary layer at the height  $y=k$ .

For three-dimensional (3-D) type of disturbances, meaning that the roughness elements cause horseshoe vortices behind the elements, critical roughness Reynolds numbers is reported in the range of 175 up to a bit over 1000. The lower value of 175 is found in [8] for a zigzag tape. Klebanoff, Schubauer and Tidstrom. [16] reported critical  $R_k$  for flat plate flow to be varying between 490 and 890 for spheres with different spacing between the roughness elements. They also state that once a three-dimensional roughness element has reached the critical height, then transition moves very close to the tripping device.

Data for  $R_k$  can also be found in [13] and [14]. It can be seen that for small  $R_{\delta^*}$  (or  $R_{\theta}$ ) a higher value of  $R_k$  is needed in order to produce transition than is needed for larger  $R_{\delta^*}$ . Gibbings, Goksel and Hall also report that in a flow with a pressure gradient, the critical  $R_k$  is slightly higher and that this effect is seen for favourable as well as for adverse pressure gradients.

### 4.1.2 Tests with a 0.4mm high transition tape and a change to a height of 0.2mm

In the first session (autumn 1998) a transition tape thickness of 0.4mm was used. These tests showed a large difference in pressure distributions between the smooth airfoil and the transition tape case even for relatively low angles of attack (5°- 8° angle of attack). The oil flow visualisation showed that the separation moved upstream substantially with the transition tape, and more than expected. It was then discussed whether this 0.4mm tape caused an extra thickening of the boundary layer, besides desirable tripping, and that this extra thickening caused the boundary layer to separate earlier. The aim was to have just a minimum thickness to cause transition, but not to cause an unwanted extra boundary layer thickening. Calculations of critical height was therefore carried out and it was found that a thinner tape (0.2mm) would result in a  $R_k$  slightly above 1000 which was thought to be, with some margin, sufficient. However, after the tests a bug in the program estimating critical  $k$  was found. The bug resulted in an overestimated  $R_k$  and the corrected calculations indicated a lower  $R_k$ . Whether the 0.2mm tape was thick enough is discussed in the subsequent sections.

### 4.1.3 Determine the roughness Reynolds number for the 0.2mm tape.

Calculations of the roughness Reynolds number based on thickness  $k=0.22\text{mm}^2$  was reconstructed after the appearance of the bug. By means of the airfoil analysis code XFOIL [17] the boundary layer quantities were calculated. The XFOIL calculations were made with free transition. By using the XFOIL<sup>3</sup> data ( $\delta^*$  and  $\theta$ ) Polhausen velocity profiles were constructed to derive the roughness Reynolds number  $R_k$ .  $R_k$  at the

---

<sup>2</sup>As mentioned in section 2.3 the actual tape height was measured to be around 0.23 mm. The calculation here is based on a 0.22 mm height. When in subsequent text it is referred to the 0.2mm tape, it is meant the tape that was measured to be around 0.23 mm high.  $R_k$  will vary slightly with  $k$ . A calculation with a height of  $k=0.2\text{mm}$  gives  $R_k \approx 500$  and  $k=0.23\text{ mm}$  gives  $R_k \approx 650$ .

<sup>3</sup> Calculations with XFOIL were made at such angles of attack that the pressure distributions upstream of the transition tape matched the measured pressure distributions. For the 15° case, the measured pressure distribution best correlates with XFOIL free transition calculations at around 10° angle of attack.

transition tape position varied only slightly for angles of attack between  $8^\circ$  and  $15^\circ$ . For the suction side,  $R_k$  was determined to 600 at  $x/c=0.034$  ( $\approx$ middle of the tape). Thus, this was lower than what was intended (around 1000).

The Reynolds number based on  $\delta^*$  at the transition tape was derived to be around 500 for  $8^\circ$  angle of attack and around 800 for  $15^\circ$  angle of attack. The ratio of tape height to boundary layer height,  $\delta^*/k$ , was calculated as being around 0.5. For both angles of attack, the parameterised stability calculations used in XFOIL predicted that linear amplification of Tollmien-Schlichting waves had started upstream of the transition tape position, thus indicating the tape being downstream of the point of neutral boundary layer stability.

For the pressure side,  $R_k$  was calculated to be around 280 at  $x/c=0.31$  with a tape thickness of 0.22 mm and the Reynolds number based on  $\delta^*$  was calculated to be around 600.

Comparing the calculated  $R_k$  to required  $R_k$ , as obtained from literature the tape height of 0.22 mm is on the margin to provoke transition. Whether it causes transition or not depends on which values of measured required  $R_k$  that are used. There is also some uncertainty in the calculated values of  $R_k$  of the current test since it is based on calculated and not on the measured pressure distributions. The question is if the height of 0.22 mm was sufficiently high to cause immediate transition?

#### 4.1.4 Expected transition position

##### **On the suction side**

For  $k=0.22$  mm  $R_k \approx 600$  and this is higher than the critical  $R_k$  of 175 given by Boermans and Waibel [8]. However, they had the tape located at  $x/c \approx 0.75$  on the pressure side of a glider wing. The tape was placed in nearly zero pressure gradient just upstream of a pressure recovery in order to avoid the extra drag associated with a laminar separation bubble. This is not the same condition as we have.

We have the tape in a region with a positive pressure gradient and the boundary layer is relatively thin. Both conditions requiring an increase in  $R_k$  and thicker boundary layers [13]. Our estimated  $R_k \approx 600$  is higher than the critical  $R_k$  of 175 given in [8] but is it high enough?



Due to lack of time and available resources during the test the transition position was never fully examined.

Figure 19 shows a larger variation in the spanwise variation with the  $k=0.2\text{mm}$  tape than with the  $0.4\text{mm}$  tape. One possible explanation could be that the  $0.4\text{mm}$  tape caused transition right at the tape<sup>4</sup> for all spanwise positions, whereas for the  $0.2\text{mm}$  tape, transition occurred some small distance downstream of the tape. The variations may be due to some small variation in tape thickness. It could also be that the  $0.2\text{mm}$  tape was sufficiently high to cause immediate transition and that the observed smaller spanwise variations were caused by another effect. The fact that the  $0.4\text{mm}$  tape is of the same thickness as the boundary layer and the tape could affect the flow in other ways than just to cause premature transition has to be mentioned.

Figure 25 shows the pressure distribution for the smooth airfoil and the airfoil with the transition tape  $0.4\text{mm}$  and  $0.2\text{mm}$  at  $8^\circ$  angle of attack. These pressure distributions indicate slightly more separation for the case with the thicker tape compared to the thinner tape. This could have two explanations, or possibly a combination of these:

1. Transition is further downstream for the case with  $0.2\text{mm}$  tape
2. Transition is at almost the same position for both tapes, but the thicker tape has influenced the boundary layer so that separation is brought upstream.

---

<sup>4</sup>  $R_k \approx 2000$  for the  $0.4\text{mm}$  tape (both for  $\alpha=8^\circ$  and  $\alpha=15^\circ$ ) so that this tape caused transition very close to the tape.

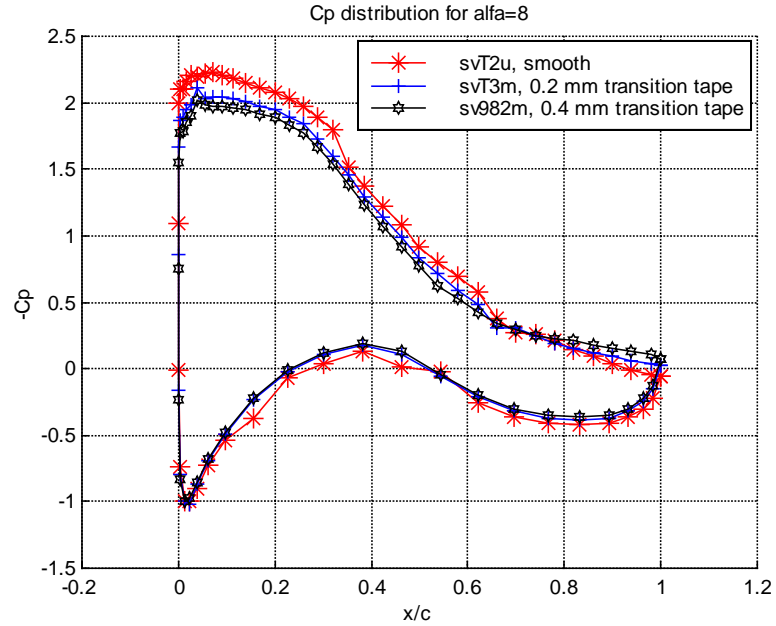


Figure 25. Pressure distributions at  $8^\circ$  angle of attack. Smooth airfoil and conditions with transition tape

In the tests with the same airfoil in 1993 [18] another transition tape was used. A tape with thin bulges with a height of  $\approx 0.4\text{mm}$  was applied at  $x/c=0.05$ . These tests were carried out at a higher Re of 1.7 million (based on chord).  $R_k$  for this tape was of the order of 1500 so that this tape should have caused transition very close to  $x/c=0.05$ .

Figure 26 shows the pressure distribution for  $8^\circ$  angle of attack. It indicates that the separation is weaker for the 1993 test case than for both current cases with the transition tapes applied at  $x/c=0.026$ . The higher Reynolds number in 1993 test case should in itself reduce the extent of separation compared to otherwise equal conditions at a lower Reynolds number. Apart from this Re-effect, it seems likely that the larger extent of separation for the cases with tape at  $x/c=0.026$  was caused by the transition point being more upstream than for the 1993 case. This indicates that even the thin tape of  $0.2\text{mm}$  has been high enough to cause transition close to the tape, at least upstream of  $x/c=0.05$  which was the position of the transition tape in 1993.

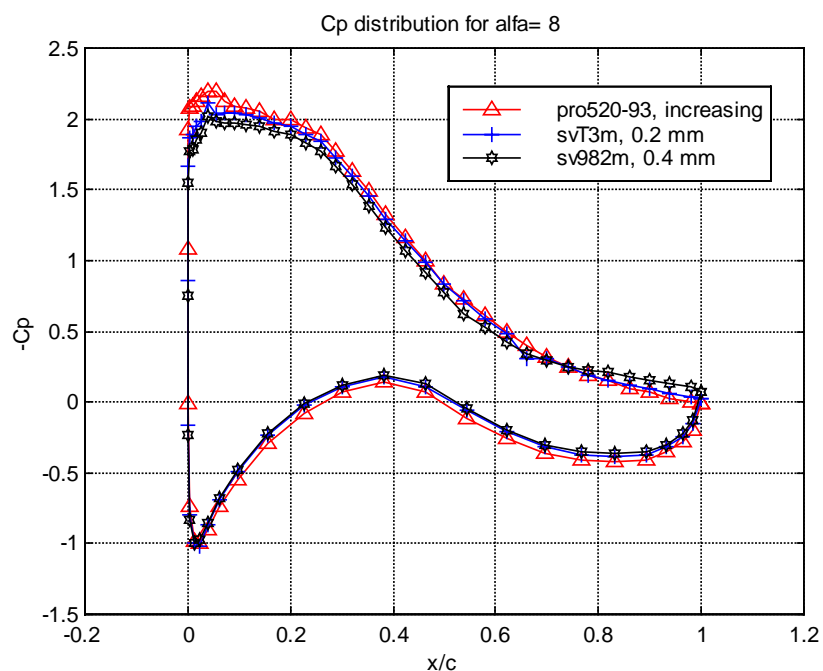


Figure 26. Pressure distributions at  $8^\circ$  angle of attack for three different transition tapes.

For  $15^\circ$  angle of attack, the pressure distributions with the two tapes 0.4mm and 0.2mm are shown in Figure 27. It is seen that these pressure distributions agree rather well. Looking at more pressure distributions for the same cases a small spread in the pressure distributions from run to run is found. Looking at all the pressure distributions obtained during the tests, it seems as if the plateau is slightly longer (separation more upstream) for the case with the thinner tape, but the differences are of the same order as the spanwise variations so no further conclusions are drawn.

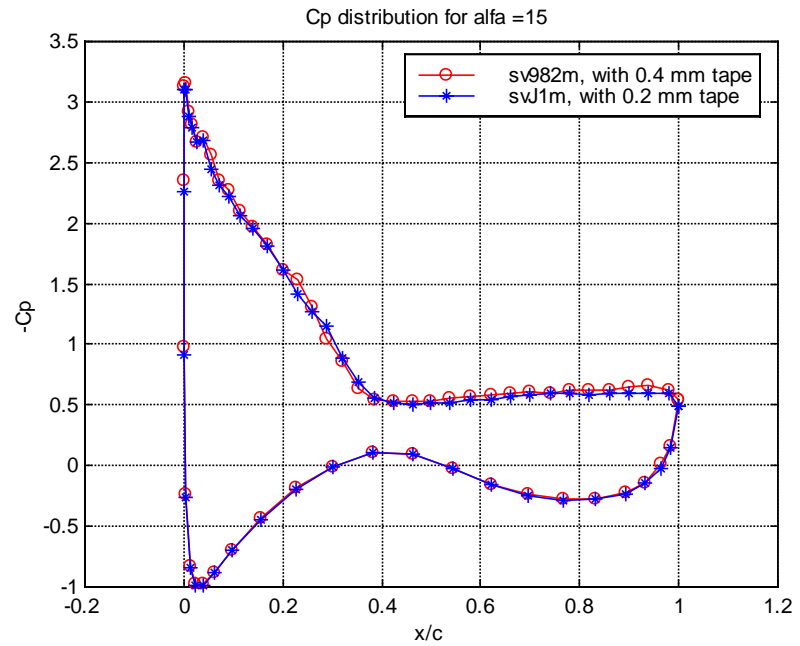


Figure 27. Pressure distributions at  $15^\circ$  angle of attack. Different transition tape thickness.

Figure 28 shows the pressure distribution from 1993 compared to the current test with the 0.2mm tape and the smooth airfoil case (as a reference). The tests in 1993 were carried out for continuously (but slow) increasing and decreasing angle of attack (sweep). Comparing the two pressure distributions for forced transition and increasing angle of attack it seems that the separation occurs at the same chordwise position. This indicates that the 0.2mm tape has been high enough to cause transition close to the tape, at least as far upstream as in the 1993 case ( $x/c=0.05$ ).

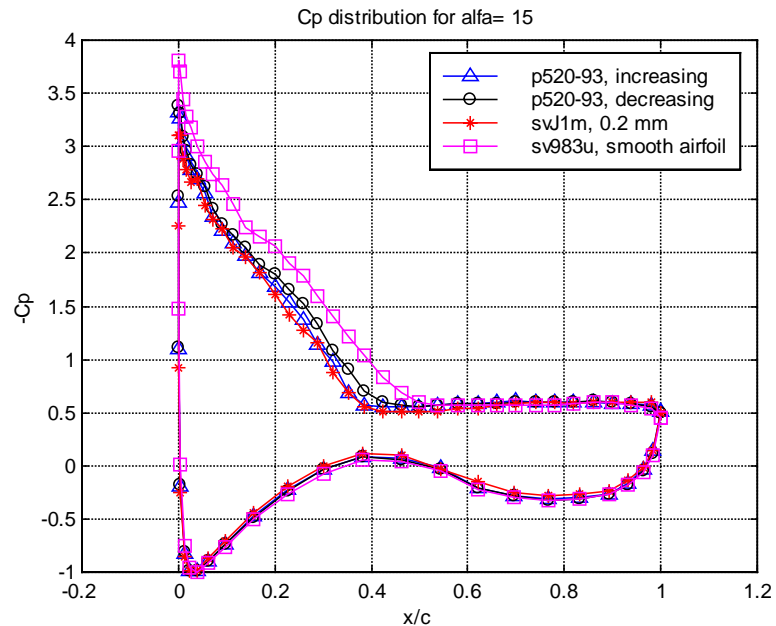


Figure 28: Pressure distributions for  $15^\circ$  angle of attack. Pressure measurements from 1993 compared to measurements in 1999 with 0.2mm transition tape and smooth airfoil.

Summarised it thus seems likely that the 0.2mm high transition tape has been high enough to cause transition close to the tape.

### On the pressure side

A similar comparison for the pressure side cannot be made since the turbulent boundary layer is well attached to the trailing edge. During the current tests the transition tape was placed at  $x/c=0.31$ . If the tape was too low to cause transition, then transition was likely to occur as free transition in a small laminar separation bubble shortly after the half chord. With free transition, the boundary layer on the pressure side would be thinner than with forced transition and the drag would be slightly lower. On the other hand, the drag contribution from the pressure side is small compared to the drag contribution from the suction side. It is believed that, regardless of the pressure side transition tape having caused transition close to the tape the influence on the pressure distribution on the suction side is small. With a calculated  $R_k \approx 280$  compared to measurements of required  $R_k$  for a zigzag tape of 175 by Boermans and Waibel [8], the tape is likely to have provoked transition, although the margins in this statement are small.

## 4.2 Error and uncertainties in the pressure measurements

As mentioned earlier there were some unclear, rather random, variations in the pressure measurements. Steps were taken to reduce the uncertainties, but without success. However, repeated measurements were carried out in order to achieve representative pressure distributions.

These “jiggles” in the pressure measurements were either due to some physical problems or grounding problem. Problems caused by blocks or leaks in the pressure equipment were examined and in order to reduce the grounding problem the measurements were only carried out with the laser turned off. With the laser running a direct impact was seen on e.g. the surrounding lighting (flickering effect). This was presumably due to the power from the laser as it accumulated energy in the laser cavity before firing the laser beam.

Figure 29 shows two pressure measurements for 15° angle of attack. The discrepancies between the two distributions are mainly on the suction side whereas these two are almost identical on the pressure side.

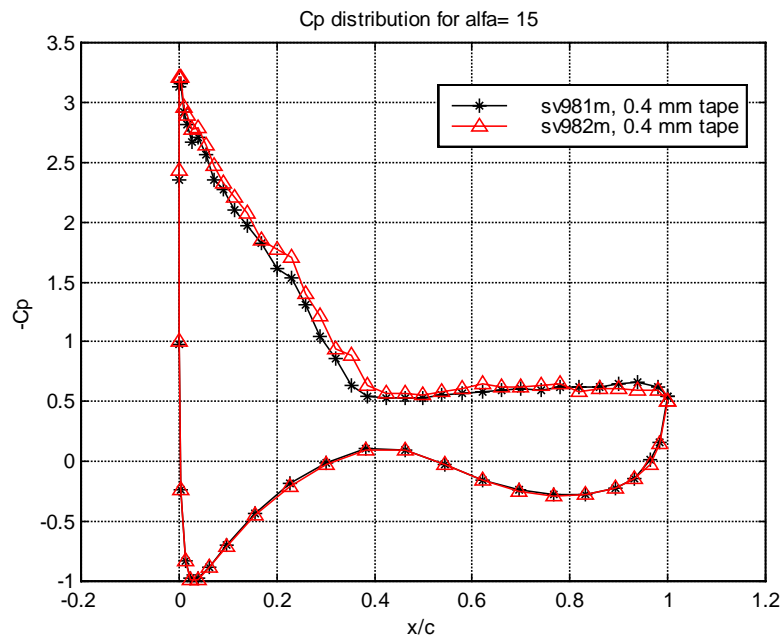


Figure 29: The pressure distribution for two similar cases showing the uncertainties in the distribution. The variation was less than the range of the max and min in the measurements showed in Figure 9.

It was, however, not like this in all the cases. Some “jiggles” were to be seen at certain taps, although it was not fixed and could vary with the measurements. An interpolation could have been used in those cases, but it was not. Examples of “jiggles” can be seen in Figure 30 at  $x/c \approx 0.7$  on the suction side and at  $x/c \approx 0.5$  on pressure side. The disagreement at the leading edge ( $x/c = 0-0.1$ ) is not fully understood but must be due to some other reason, possibly some occasional, slightly different angle of attack. However, they are from two different setups, sv983u, first session (autumn 1998) and svT2u, second session (spring 1999). It shows some repeating behaviour of the pressure measurements.

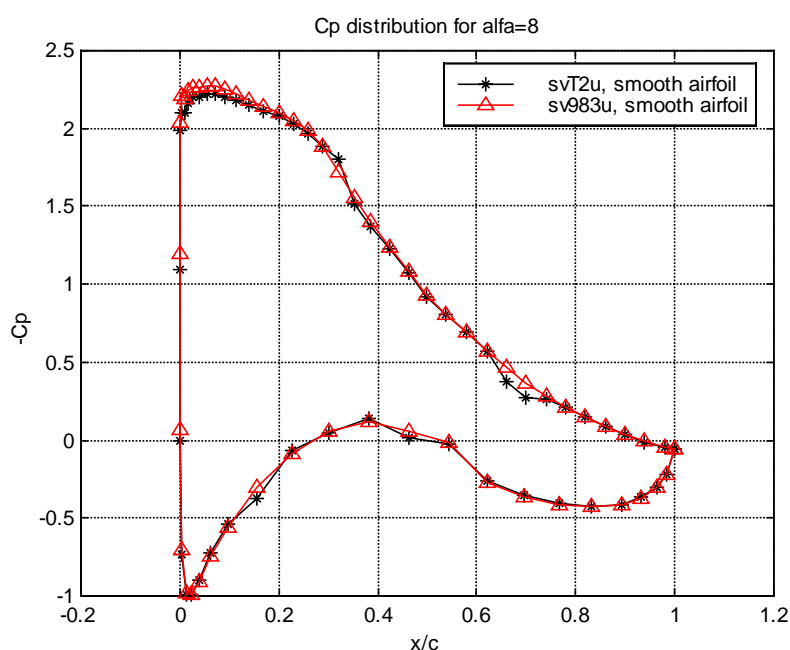


Figure 30: Two pressure distributions for  $8^\circ$  angle of attack, one from the first session and the other from the second session.

## 4.3 Error and uncertainties in the PIV-results

### 4.3.1 Scale factor, offset and alignment

#### *Scale factor*

The scale factor was determined by using a millimetre mesh paper at the laser sheet position, which when photographed with the PIV camera gives a conversion factor from pixels to millimetres.

Since approximately 100-200 mm of the mesh paper was used in the scale picture and the scale lines were located within 0.5mm, the error in the scale factor should be less than 0.5%. This error would, apart from giving the wrong positions for vectors away from the reference point on the plate surface, give an erroneous scaling of the velocities measured.

#### ***Offset and alignment***

The position (offset) and alignment of the image was also determined from the scale picture. In all cases the aim was to align the examined image areas, so that they were parallel to the chordwise direction. To minimise the error produced by a wrong alignment close to the separation point, the offset was calculated at  $x/c=0.393$  in the cases where this position was within the scale picture. In other cases a chordwise position (x-position) close to the centre of the picture was chosen for estimating the offset. The offset in the x-direction was measured in the scale picture, while the y-offset was obtained from the actual PIV measurement images, where the airfoil surface was visible as a bright line due to the reflex in the surface. The error in the x-position may be as large as 1%, while the y-position should be accurate within 0.5% at the reference point as it is especially important when determining the boundary layer parameters. A particular problem in the determination of this offset was that the reflex region near the surface was up to 1.3mm wide in the image. Within these limits the y-offset was chosen to give an attached boundary layer (i.e.  $U_{//}=0$  at the plate when extrapolating from measurements farther out) in areas where this was expected, otherwise the centre of the region was chosen as the airfoil surface.

### **4.3.2 Velocity discretisation<sup>5</sup> and velocity gradients**

Unfortunately, the software (FlowMap) used in the present study seemed to give semidiscrete velocity distributions. Velocities that corresponded to particle movements of an integer number of pixels between the exposures were more common than the in-between velocities. Probably caused by some kind of failure of the subpixel interpolation. The subpixel interpolation was used to determine the exact centre of a particle to give a higher spatial resolution than one pixel. This discretisation would probably not affect the mean velocities, but the perturbation velocities and the statistical moments based on these will be questionable. Since the discretisation was generally rather coarse (5m/s in case J4), this error was significant. In Figure 31 the probability density functions (PDF) of  $u$  in

---

<sup>5</sup> Discretisation, see Computational Fluid Dynamics, J.D. Andersson, McGRAM-HILL1995



the vicinity of the separation position are presented. Since there is a relatively low number of samples per discrete level if only one single point in space was considered, a distribution of the statistics from several (15) points has been created. This made the discretisation more evident since the relative influence of random variations gets lower. The left Figure shows a velocity distribution obtained while the mirror was in place and the right one without mirror. As can be seen, the discretisation actually gets less severe in the latter case, even though the picture was slightly sharper in this case. (S is the physical size one pixel appears to have in the camera image). In the former case, the velocity discretisation is 4.48m/s and in the latter is 5.03m/s.

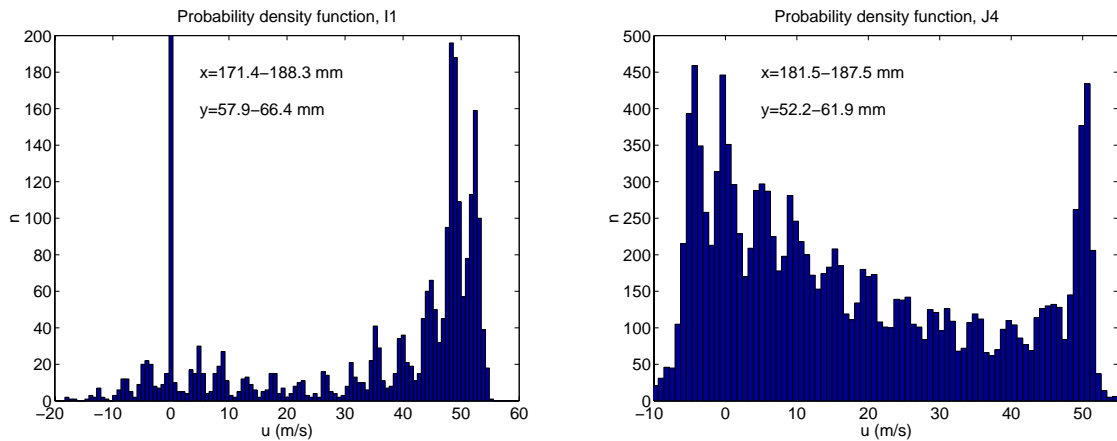


Figure 31: The probability density function showing the velocity discretisation in the results of the program. The discretisation in the left Figure case was determined to  $S=0.179$  mm,  $\Delta t=40\mu s \Rightarrow \Delta u=4.48$  m/s, whereas determined to,  $S=0.075$  mm,  $\Delta t=15\mu s \Rightarrow \Delta u=5.03$  m/s in the right figure.

Another aspect to consider is the velocity gradients. In areas where there was a significant velocity gradient (a large range of mean velocities over the interrogation area) the measured mean velocity was tended to be lower than the actual mean velocity in that area. The reason for this is that the high speed particles will have a greater tendency to leave the interrogation area between the exposures than the slower particles. As a rule of thumb, the requirement suggested by Keane and Adrian [11] may be used:

$$\frac{\Delta u \Delta t}{Sd} < 0.03$$

$\Delta u$ : maximum mean deviation from the average velocity in an interrogation area

$\Delta t$ : time between exposures

$S$ : object-to-image scale factor (m/pixel)

$d$ : side length of the interrogation area in pixels

*E.g. at  $x=150$  mm in run J4, the variables in the above relation are estimated at  $\Delta u=12$  m/s,  $\Delta t=15$   $\mu$ s,  $S=75.4$   $\mu$ m/pixel,  $d=32$  pixels, which gives a left-hand side of 0.075. This suggests that there may be some underestimation of the mean velocity in this case. For the relation to hold, the mean velocity deviation over an interrogation is as in this case cannot be more than 5 m/s, which corresponds to a velocity gradient of 4000  $s^{-1}$ .*

### 4.3.3 Errors due to the post processing of the PIV data

#### 4.3.3.1 Validation

To check the sensitivity of the results depending on how the PIV data were validated, several slightly different but reasonable validation criteria were tested. The case labelled in Table 4 below is the validation that was used throughout this study. This is described in section 2.8. The fact that the validation in each point depends on the local mean and rms velocities means that a much smaller range of velocities is accepted in the free-stream than in the boundary layer with its large velocity fluctuations. To check the sensitivity of the results for different validation criteria, the J4 case was run with a narrower validation window ( $2 \times \text{rms}$ ) (case b) and with the imported validation only (case c), see Table 4.

Table 4: The resulting sensitivity due to different validation in the post processing. Case a.  $U \pm 3u_{\text{rms}}$ , case b.  $U \pm 2u_{\text{rms}}$ , case c. imported FlowManager validation

Validation	$x_s/c$	$H(x_s)$	$\delta^*(x/c=0.422)(\text{mm})$
a	0.359	3.1	10.7
b	0.357	3.3	10.6
c	0.358	3.0	10.8

As the Table shows, the effect of changing the validation criterion is negligible. To demonstrate what these validation criteria implicate when it comes to actual measurement results, two probability density functions from the J4 run are given Figure 32. These distributions are based on the vectors that have passed the FlowManager range and peak value ratio validations. The left one shows the velocity distribution near the plate in the separated region, whereas the right one shows the conditions in the free stream. One observation made in the probability density functions (pdf's), is that close to separation, the velocity distributions are a skew and the validation criterion used may result in too many correct positive velocities being discarded while at the same time erroneous negative velocities are accepted. It is also obvious that the global range validation performed in FlowManager, which has to be adjusted to accept the high velocities of the free-stream, is unable to reject unreasonably large vectors in the separated region.

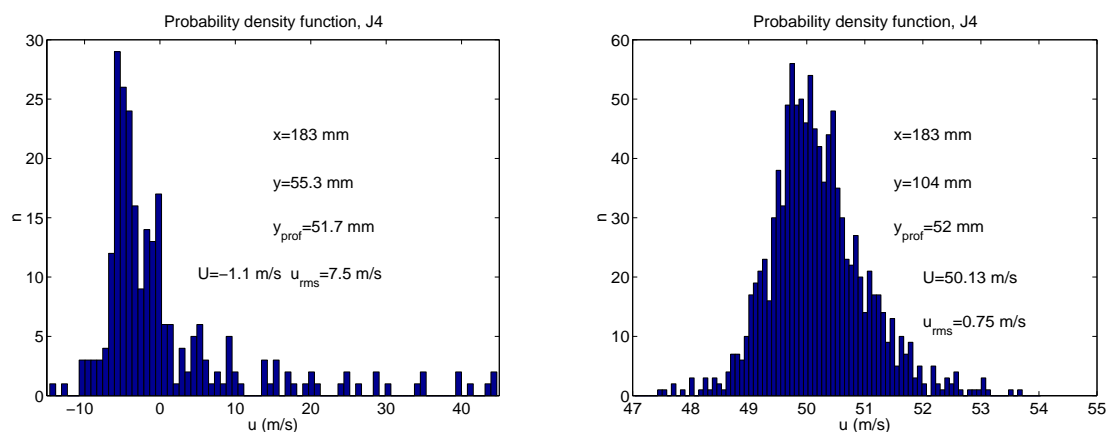


Figure 32. Probability density functions. Left figure: in a separated region. Right figure: outside of the boundary layer.

#### 4.3.3.2 Smoothing

The smoothing, which was applied to the mean velocities that is described in the section 2.8, has the undesired effect that the strong velocity gradients found in the boundary layer are somewhat dampened. Figure 33 below shows the effect the smoothing has on a velocity profile close to separation. In this case, the shape factor decreased from 3.47 to 3.15 because of the smoothing procedure.

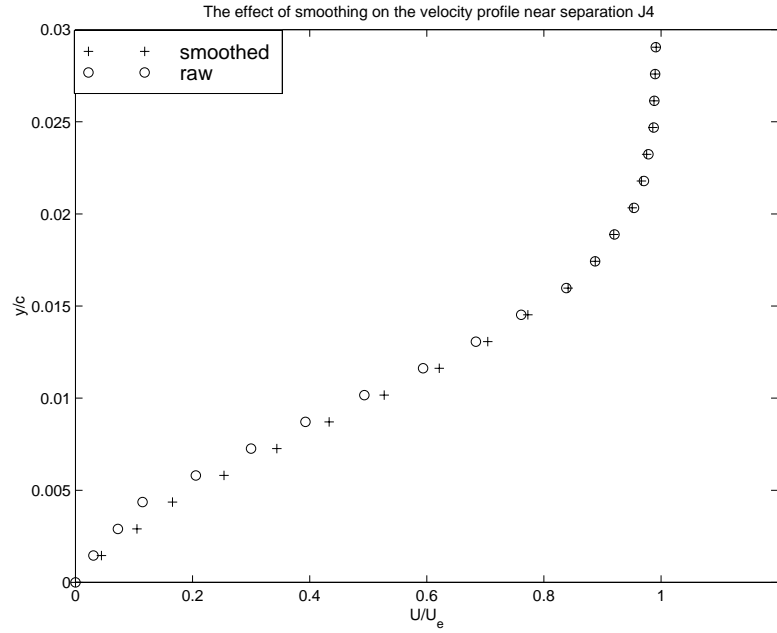


Figure 33. Mean velocity profiles with and without smoothing near separation.

Since the back-flow coefficient, which was used for determining the separation position, was not smoothed, it was not affected by the smoothing.

#### 4.3.3.3 Extrapolation

Since it was of vital interest in this study to find the position where the boundary layer separates, the velocity field and back-flow coefficient were extrapolated towards the surface (the back-flow coefficient was used as a separation criterion). As Dengel and Fernholz [10] showed, the back-flow coefficient tends to increase rapidly close to the plate. Three different functions were tested for their ability to accurately model  $\chi(y)$  in order to extrapolate data close to the plate:

- $\chi(y) = ky + \chi_w$
- $\chi(y) = k_2 y^2 + k_1 y + \chi_w$
- $\chi(y) = \chi_w e^{-ky}$

To obtain the constants used in these, the validated  $\chi(y)$  at the y-positions closest to the plate were used. For case a) and c), two values were used

and for case b) three values were used. Table 15 shows the separation positions obtained by the three cases in the PIV J4 test case.

Table 5: The result by using different extrapolation functions of description of the back-flow coefficient.

method	$x_s/c$	$H(x_s)$
a	0.359	3.07
b	0.359	3.07
c	0.358	3.04

In Dengel and Fernholz [10] it is indicated that  $\chi_w$  can be linearly extrapolated towards the wall if the  $\chi$ -value obtained, closest to the wall, is at least 25%. This is true close to separation, so the simple linear extrapolation was chosen for the rest of this study. As Table 5 demonstrates, the difference between different extrapolation functions was negligible. The separation position was determined through linear interpolation between these extrapolated values near the surface, as Figure 34 indicates. However, only the back-flow coefficients that were considered reliable and close enough to 0.5 to make the linear extrapolation applicable were used.

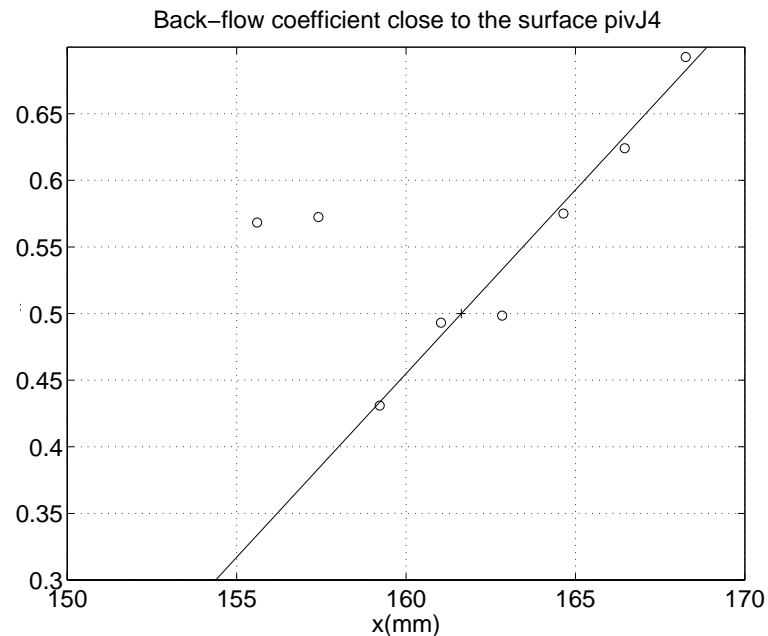


Figure 34: The extrapolated value of back-flow coefficient down to the surface.

#### 4.3.3.4 Temporal variations

The variation of the separation position (line) over time was estimated by plotting subsets (100 image pairs) of the PIV data in test case J4. The results were compared in order to examine how much the averages of these subsets differ from one another. As Table 6 shows, the position of the mean separation point varied over a range of about 10 mm ( $x/c=0.022$ ) over time. This is considered to be small enough to make it seem reasonable that the acquisitions of around 1000 image pairs would result in a reliable mean value of the separation position. The 100 recordings in each series in Table 6 were normally acquired over a period of 1 minute.

Table 6: The temporal variation of separation position and boundary layer parameters for the PIV data case J4.

samples	$x_s/c$	$\delta^*$ [mm]	$\theta$ [mm]
0-99	0.387	9.03	1.85
100-199	0.398	8.1	2.03
200-299	0.393	8.09	2.08
300-399	0.393	7.66	1.93
400-499	0.387	8.41	1.65
500-599	0.398	8.69	1.76
600-699	0.389	8.69	1.88
700-799	0.393	8.71	1.73
800-899	0.389	9.12	1.82
900-999	0.373	9.58	1.7
1000-1099	0.397	8.19	1.94
	0.387 $\pm$ 0.0133	8.6 $\pm$ 1.0	1.87 $\pm$ 0.22

#### 4.3.4 Determination of the free-stream conditions

To get some idea about the free stream turbulence level of the wind tunnel, PIV measurements were made after the airfoil model had been removed from the test section. This made it possible to a direct comparison of the free stream velocity derive by pressure measurements and PIV measurements. Unfortunately, the coarse velocity discretisation that was found in the PIV measurements, even though an offset of 32 pixels was used between the two image pairs, makes it hard to estimate the velocity fluctuation ( $u_{rms}$ ) accurately. The offset was used to increase the velocity resolution around the expected mean velocity and make the velocity discretisation smaller. The discretisation was found to be 1.37m/s. The turbulence intensity at  $U=40\text{m/s}$  had been found to be around 0.15%, see section 2.1. That would give an  $u_{rms}$  of approximately 0.06m/s, which is much smaller than the velocity discretisation.

This means that the error in  $u_{rms}$  determined by PIV may be significant in this low turbulence case. Figure 35 shows the free-stream probability density function for the case K1, where the offset was one interrogation area (32 pixels).

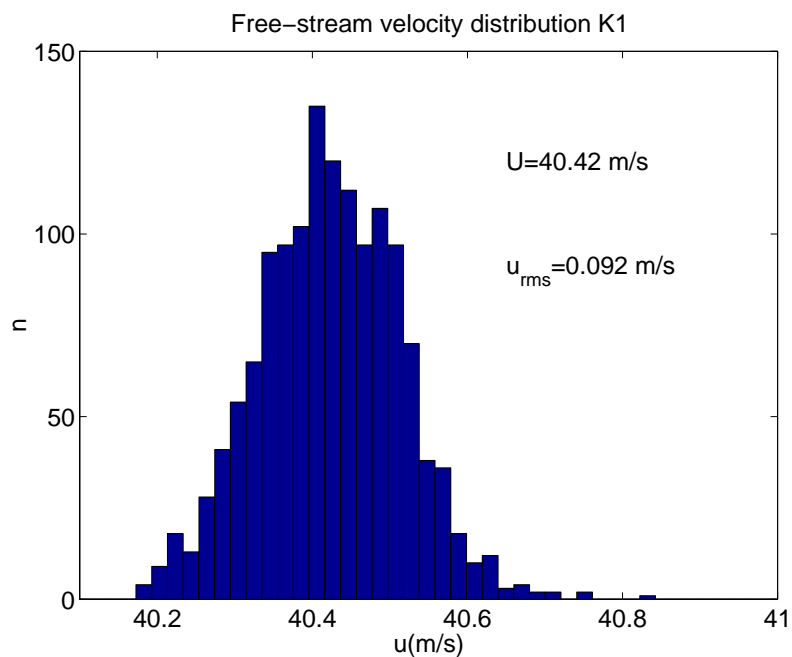


Figure 35. The figure shows the probability density function of the free stream measurements

The experiment K1 gave  $U=40.42\text{m/s}$  and  $u_{rms}=0.092\text{m/s}$ , i. e a free stream turbulence level of 0.23%. The free-stream mean velocity determined by the pressures measurements was  $40.26\text{m/s}$ , i.e. 0.4% lower.





## 5 Conclusions

The purpose was to study the flow field around the FFA-W3-211 airfoil. Oil flow visualisation, pressure measurements and PIV measurements were used to examine the flow field.

- The flow field was determined by PIV and available for comparison with CFD-results.
- Based on the velocity field obtained by PIV measurements the separation position, the velocity profile at different chordwise positions and boundary layer quantities were derived
- The separation position, for 15 ° angle of attack, was determined to  $x/c=0.39\pm0.03$  in the PIV measurements, in the pressure measurements to  $x/c=0.40\pm0.05$  and somewhat subjectively in the oil flow to  $x/c\approx0.42$ .



## References

- [1] P. Fuglsang et.al “Wind Tunnel Tests of the FFA-W3-241, FFA-W3-301 and NACA 63-430 Airfoils”  
Risø-R-1041(EN)  
Risø, Denmark 1998
- [2] W.Kühn “EUROPIV: A cooperative action to apply Particle Image Velocimetry to problems of industrial interest”  
Contract No: BR.PR-CT95-0118  
Report no 16PT02, France 1998
- [3] K.Sjörs “Tests of seeding particles for PIV in wind tunnel LT1”  
FFA TN 1998-20  
Bromma, Sweden 1998
- [4] A. Björk “2-D airfoil wind tunnel test at stall”  
Proceedings of IEA 7<sup>th</sup> Symposium on aerodynamics of wind turbines, Technical university of Denmark  
29-30<sup>th</sup> November 1993, Denmark
- [5] W.H.Rae,JR  
A.Pope “Low-Speed Wind Tunnel Testing”  
A Wiley-Interscience publication  
New York , USA 1984
- [6] S.A. Yon and J. Katz “Study of the Unsteady Flow Features on a Stalled Wing”, AIAA Journal, Vol 36, No. 3, March 1998
- [7] H.Schlichting “Boundary Layer Theory”  
McGraw-Hill Book Company  
1960
- [8] L.M.M. Boermans  
and G. Waibel “Aerodynamic and structural design of the standard class sailplane ASW-24”,  
Proceedings of ICAS conference 1988,  
ICAS-88-2.7.2 (pages 969-978)
- [9] G Lidén et al “Koncentrationen partikulär propylenglykol vid användning av rökgenerator i samband med TV-inspelning”  
National Institute of Occupational Health, Sweden, 1988
- [10] P.Dengel  
H.H.Fernholz “An experimental investigation of an incompressible turbulent boundary layer in the vicinity of separation”  
Journal of Fluid Mechanics 212 (1990)

- [11] Keane R.D.  
Adrian R.J.      “Theory of cross-correlation analysis of PIV images”  
Applied Scientific Research 49 3 1992
- [12] J.G. Gibbings,  
O.T. Goksel and  
D.J. Hall      “The influence of roughness trips upon  
boundary layer transition, Part 1  
Characteristics of wire trips”, Aeronautical  
Journal, October 1986
- [13] J.G. Gibbings,  
O.T. Goksel and  
D.J. Hall      “The influence of roughness trips upon  
boundary layer transition, Part 2  
Characteristics of single spherical trips”,  
Aeronautical Journal, November 1986
- [14] J.G. Gibbings,  
O.T. Goksel and  
D.J. Hall      “The influence of roughness trips upon  
boundary layer transition, Part 3  
Characteristics of rows of spherical transition  
trips”, Aeronautical Journal, December 1986
- [15] D.I.A. Poll      “The Effect of Isolated Roughness Elements  
on Transition in Attachment-Line Flows”,  
Laminar-Turbulent Transition, Edited by D.  
Arnal and R. Michel, Springer-Verlag,  
IUTAM Symposium Toulouse France  
September 11-15, 1989
- [16] P.S. Klebanoff,  
G.B. Schubauer  
and K.D. Tidstrom      “Measurements of the Effect of Two-  
dimensional and Three-dimensional  
Roughness Elements on Boundary-Layer  
Transition”, Journal of the Aeronautical  
Sciences, November 1955, 22, 11, 803
- [17] M. Drela      “XFOIL-An analysis and design system for  
low Reynolds number airfoils”, Low  
Reynolds Number Aerodynamics,  
Proceedings of the conference in Notre  
Dame, In, USA, 1989, Springer-Verlag
- [18] A. Björck      “A Guide to data files from wind tunnel test  
of a FFA-W3-211 airfoil at FFA”, FFA-V-  
019, FFA The Aeronautical Research  
Institute of Sweden, Bromma, Sweden March  
1996

## Acknowledgement

The authors would like to acknowledge the Swedish National Energy Administration for the financial support. The authors would also like to acknowledge Ms. Barbro Muhammad-Klingmann and the staff at the Department of Fluid Mechanics at the Royal Institute of Technology in Stockholm for their support during this study.



## Appendix 1      A guide to the data

This is a guide to the data. It includes the evaluated data from pressure measurements and PIV measurements.

### **The pressure measurements**

*A comment on how the raw pressure data were created:*

The acquisition program (written in LabView) determined mean, standard deviation, min and max for each channel (equivalent to a transducer). The sampling frequency was either 830 Hz during 0.3 seconds or 73 Hz during 10 seconds. This acquisition procedure was then repeated for every Scanivalve step (48 connections). Thus, a pressure raw data file consisted of 48 rows and two zero-measurements before and two zeros after the test run. The waiting time, before acquiring data (after the Scanivalve has made a step), was chosen between 0.1-5 seconds. This waiting time was introduced to reduce transient influence on the result. Since the acquisition program was developed in between the two test sessions, the first version only included mean and standard deviation and not mean, standard deviation, max and min as in the final version .

The evaluated pressure data files (column 7 in Table 9) was built up for increasing angle of attack. Those are specified in Table 7 and correspond to the pressure measurements acquired during the spring session 1999.

The acronym for these files is **svXYZ**, where

- **X** = is a letter corresponding the day as in the PIV data except T for Test
- **Y** = a log number
- **Z** = is either m= with transition tape or u= smooth airfoil.

The equivalent Table for the autumn session is shown in Table 8. The data included not in max and min as mentioned above. The acronym for the 1998 files is **sv98YZ**. The Table 9 shows the complete pressure measurements files.

Note; The extension **A.txt** on the file name indicates ASCII-format file. The others are, by default, Matlab format files (**.mat**).

Table 7: The description of the column quantities of the spring session

Quantities	units	index columns	comments
alfa	degrees	1	angle of attack
cl		2	lift coefficient
cd		3	drag coefficient
cp_0(1:58)		(4:61)	cp =pressure coefficient_ midspan
cp_100(1:5)		(62:66)	_100 mm off midspan
cp_500(1:4)		(67:70)	_500 mm off midspan
cp_17(1:48)		(71:118)	_pressure tap # 17( or # 13), time average
cp_20(1:48)		(119:166)	_pressure tap # 20, time average
cp_0std(1:58)		(167:224)	_standard deviation midspan
cp_0min(1:58)		(225:282)	_min midspan
cp_0max(1:58)		(283:340)	_max midspan
cp_17std(1:48)		(341:388)	_standard deviation # 17 (or #13)
cp_17min(1:48)		(389:436)	_min # 17 (or # 13)
cp_17max(1:48)		(437:484)	_max # 17 (or # 13)
cp_20std(1:48)		(485:532)	_standard deviation # 20
cp_20min(1:48)		(533:580)	_min # 20
cp_20max(1:48)		(581:628)	_max # 20
pf(1:4)	Pa	(629:632)	wall pressure fore cross-section ( ceiling, starboard, floor, port)
pa(1:4)	Pa	(633:636)	wall pressure aft cross-section ( ceiling, starboard, floor, port)
mean(q)	Pa	637	mean dynamic free steam pressure
mean(T)	K	638	mean temperature in test section
P	Pa	639	total pressure
mean(Re)		640	Re number



Table 8: The column description of the autumn session in 1998.

Quantities	units	index columns	comments
alfa	degrees	1	angle of attack
cl		2	lift coefficient
cd		3	drag coefficient
cp_0(1:58)		(4:61)	cp =pressure coefficient_ midspan
cp_100(1:5)		(62:66)	_100 mm off midspan
cp_500(1:4)		(67:70)	_500 mm off midspan
cp_13(1:48)		(71:118)	_pressure tap # 13, time average
cp_20(1:48)		(119:166)	_pressure tap # 20, time average
cp_0std(1:58)		(167:224)	_standard deviation midspan
cp_13std(1:48)		(225:272)	_standard deviation # 13
cp_20std(1:48)		(273:320)	_standard deviation # 20
pf(1:4)	Pa	(321:324)	wall pressure fore cross-section ( ceiling, starboard, floor, port)
pa(1:4)	Pa	(325:328)	wall pressure aft cross-section ( ceiling, starboard, floor, port)
mean(q)	Pa	329	mean dynamic free steam pressure
mean(T)	K	330	mean temperature in test section
P	Pa	331	total pressure
mean(Re)		332	Re number

Table 9: The pressure data. The evaluated files are those presented in column 7, evaluated files, the corresponding ASCII-file in column 9. The 4th column indicates if the raw data includes a zero measurements before and after the pressure measurements was carried out or not. In the cases where one or several runs were carried out without zeros before and after, the first zero in the set was used.

Autumn 1998								
Raw-data file	PC-format	total pressure [kPa]	zero fore/ after	comments	temp	evaluated file		ascii-format file
run 1			y=yes, n=no	transition tape, 830 Hz, DA=0.3s, VA=0.1s		sv981m	DA=data acquisition time, VA=waiting time	sv981mA.txt
981115_171930	p00_s1.txt	101.5	y			1		
981115_172944	pm5_s1.txt		y					
981115_173617	pm2_s1.txt		y					
981115_174514	p02_s1.txt		y			2		
981115_175650	p05_s1.txt		y			3		
981115_180348	p08_s1.txt		y			4		
981115_181326	p10_s1.txt		y			5		
981115_183016	p12_s1.txt		n			6		
981115_184225	p14_s1.txt		n			7		
981116_091359	p00_s1T.txt	101.8	y	! name				
981116_092357	p12_s1.txt		y					
981116_152320	p15_s1.txt		n			8		
981116_153041	p17_s1.txt		y			9		
981116_153708	p20_s1T.txt			only 43 colu.				
981116_155107	p20_s1.txt					10		
981116_155933	p22_s1.txt					11		
981116_161653	p25_s1.txt					12		
run 2				transition tape	13.7 - 14.6	sv982m		sv982mA.txt
981122_132107	p00_s2.txt	102.5	y			1		
981122_133404	p02_s2.txt		n			2		
981122_133712	p05_s2.txt		n			3		
981122_134013	p08_s2.txt		n			4		
981122_140053	p10_s2.txt		y			5		
981122_140733	p12_s2.txt		n			6		
981122_141446	p14_s2.txt		n			7		
981122_142003	p15_s2.txt		n			8		
981122_142551	p15_2s2.txt		n	! name				
981122_142851	p15_3s2.txt		n	! name				
981122_143123	p15_4s2.txt		n					
981122_152529	p17_s2.txt		y			9		
981122_153257	p20_s2.txt		n			10		
981122_153617	p22_s2.txt		n			11		
981122_154158	p25_s2.txt		n			12		
run 3				smooth		sv983u		sv983uA.txt
981122_162539	p00_u1.txt	102.5	y			1		
981122_163151	p02_u1.txt		n			2		
981122_163440	p05_u1.txt		n			3		
981122_164213	p08_u1.txt		n			4		
981122_165154	p10_u1.txt		n			5		
981122_165726	p12_u1.txt		n			6		
981122_170121	p14_u1.txt		n			7		
981122_170410	p15_u1.txt		n			8		
981122_170634	p15_2u1.txt		n					
981122_171002	p17_u1.txt		n			9		
981122_171306	p20_u1.txt		n			10		
981122_171610	p22_u1.txt		n			11		
981122_171954	p25_u1.txt		n			12		
981122_173255	p00_2u1.txt		y					

Spring 1999								
run 4				smooth, 830 Hz, DA=0.3s, VA=0.1s ! pressure tape #13		svT1u (old), svT2u		svT1uA.txt, svT2uA.txt
990217_181937	T00a1819.txt	97.8	y	used as "zero"		1		
990217_190642	T05a1906.txt		y			3		
990217_191353	T08a1913.txt		n			4		
990217_192451	T10a1924.txt		n			5		
990217_193303	T12a1933.txt		n			6		
990217_193731	T15a1937.txt		n			7		
990217_194423	T20a1944.txt		n			8		
990217_195219	N00a1952.txt		y			2		
run 5		99.14		transition tape, pressure tap #13	11.5-16-5	svT3m		svT3mA.txt
990223_104325	N00a1043		y			1		
990223_111242	T05b1112		n			3		
990223_111738	T05b1117		y			4		
990223_112501	T08a1125		y			5		
990223_114344	T12a1143		n			6		
990223_115039	T15a1150		n			7		
990223_115516	T20a1155		n			8		
990223_120510	N00a1205		y			2		
testrun 1		97.73		transition tape	8.7-10.8			
990224_104821	N00a1048		y	830 Hz, DA 0.3 VA= 0.1				
990224_105333	N00b1053		y	830 Hz, DA 0.6 VA= 0.2				
990224_110317	N00c1103		y	830 Hz, DA =0.6 s, VA= 0				
990224_181027	B00a1810	98.8	y	tap # 44, # 46 excluded				
testrun 2								
990225_103607	C00a1036	99.8	y	scanivalve switch		OBS kanske fel i trycket vid utv. !		
990225_164933	N00a1649		y					
990226_113851	D00a1138	99.6	y	new scanivalveconnec. ( #2)				
testrun 3		100.2						
990227_121818	E00a1218		y					
990227_122253	E00b1222		y					
990227_124656	E00c1246		y	switch tap 43 and 44				
990227_125540	E00d1255		y	switch back				

<b>run 6</b>		99.4		830 Hz, DA 0.3, VA 0.1s	13.9- 14.4	svA1m		svA1mA.txt
				transition tape, PIV at pos. B, 60 mm lens				
990303_142207	A00b1422		y			1		
990303_142656	A08b1426		n			3		
990303_143428	A08b1434		n			4		
990303_143855	A08b1438		n			5		
990303_144455	A08b1444		n	alfa =8.2 on display		6		
990303_145000	A15b1450		n			7		
990303_145418	A00b1454		y			2		
<b>run 7</b>		99.78				svC1m		svC1mA.txt
990304_143723	C00b1437		y	q=1000		1		
990304_144153	C00b1441		y			3		
990304_145000	C00b1450		y			4		
990304_145729	C15b1457		y			5		
990304_150422	C15b1504		y			6		
990304_151022	C15b1510		y			7		
990304_151822	C00b1518		y	q=500				
990304_152711	C15b1527		y	q=500				
990304_153317	C15b1533		y	q=500				
990304_154845	C15b1548		n	q=500				
990304_155142	C00b1551		y	q=1000		2		
<b>run 8</b>		99.53		Pressure tap # 17		svD1m		svD1mA.txt
990305_094024	D00b0940		y	q=1000	11.7	1		
990305_094445	D00b0944		y		12.6	2		
990305_095202	D02b0952		n		12.5	4		
990305_095551	D05b0955		n		13.9	5		
990305_095904	D08b0959		n		14.6	6		
990305_100140	D10b1001		n		15	7		
990305_100755	D11b1007		n		15.7	8		
990305_101657	D12b1016		n		16.5	9		
990305_101945	D15b1019		n		16.8	10		
990305_102243	D20b1022		n		17	11		
990305_102558	D00b1025		y		17	3		

run 9		99.58		q=500		svD2m5		svD2m5A.txt
990305_121451	D00b1214		y		10.5	1		
990305_122037	*(00)		n		11			
990305_123714	*(02)		n		11.3			
990305_124659	*(05)		n		13.2			
990305_152435	D00b1524		n		10.4	2		
990305_153026	D02b1530		n		11.8	4		
990305_153324	D05b1533		n		12.1	5		
990305_153607	D05b1536		n		12.6	6		
990305_153931	D08b1539		n		12.8	7		
990305_154222	D10b1542		n		13	8		
990305_154620	D11b1546		n		13.1	9		
990305_154927	D12b1549		n		13.2	10		
990305_155150	D12b1551		n		13.3	ej		
990305_155447	D15b1554		n		13.3	11		
990305_155721	D15b1557		n		13.3	12		
990305_160142	D20b1601		n		13.4	13		
990305_160511	D00b1605		y		13.3	3		
run 10		101.5		q=1000		svl1m		svJ1mA.txt
990310_103050	I00b1030		y	830 Hz, DA=0.3 s, VA=0.1 s	13.5	1		
990310_103801	I00b1038		y	73 Hz, DA=10s, VA=5 s	13.5-15.5	2		
990310_105843	I05b1058		y		15.5-16.7	4		
990310_113805	I08b1138		y		16.7-17.8	5		
990310_120531	I12b1205		y		16.5-18.1	6		
990310_122527	I15b1225		y		16.5-18.4	7		
990310_124513	I00b1245		y		16.3-18.1	3		

run 11		101		transition tape 73 Hz, DA=10s, VA=5s	svJ1m		svJ1mA.txt
990311_094025	J00b0940		y		13.6-15	1	
990311_102301	J05b1023		y		13.2-16.6	2	
990311_104353	J08b1043		y		16.3-17.7	3	
990311_110443	J10b1104		y		16.5-17.7	4	
990311_112351	J11b1123		y		17-17.7	5	
990311_114508	J12b1145		y		17.5-17.8	6	
990311_121603	J15b1216		y		17.1-19	7	
990311_123254	J20b1232		y		18.5-20.1	8	
run 12		101.5			svJ2m		svJ2mA.txt
990311_210544	J00c2105		y	transition tape 73 Hz	12.3-16.6		
990311_215434	J00c2154		y	smooth 73 Hz, DA =	13.1-17.9	1	
990311_221243	J05c2212		y		17.4-17.6	2	
990311_223734	J08c2237		y		17.5-18.1	3	
990311_225518	J10c2255		y		17.9-19.6	4	
990311_232205	J11c2322		y		19.4-20.5	5	
990311_233940	J12c2339	(101.7 kPa)	y		19.1-20.1	6	
990311_235717	J15c2357	(101.7 kPa)	y		20.1-21.2	7	
990312_001729	J20c0017	(101.7 kPa)	y		20.5-21.5	8	
run 13		102.1		no model in the test section			
990312_110601	K00c1106		y		13.3-16-6		
990312_112408	K00c1124		y		16.3-17,4		

### The PIV measurements

The PIV data were saved in three different ways. One as variables shown in Table 10 and in Matlab default format (.mat), the second as a tensor (42x42x7, see Table 11) also Matlab format and the last as an array in ASCII-format, see Table 12. The evaluated data filename was denoted by the acronym in Table 13 combined with the prefix “*piv*”, e.g. *pivJ4.mat*. The extension *T* denotes **tensor** and *A.txt* indicates the **ASCII-file**.

Table 10: The description of the PIV data in the first way (e.g. *pivJ4.mat*). Notice that the size of the position coordinates may shift. A check is necessary in order to be sure.

Variables	units	size	comments
xv	mm	41x1	chordwise pos.
yv	mm	42x1	pos. Normal to the chord
umean	m/s	41x42	mean velocity in the xv pos.
vmean	m/s	41x42	mean velocity in the yv pos.
urms	m/s	41x42	rms of u
vrms	m/s	41x42	rms of v
$\chi$		41x42	back-flow coefficient
okn		41x42	nb. of accepted vectors at each pos.
nFiles		1x1	nb. of runs
px	mm	58x1	coordinate for the profile, chordwise
py	mm	58x1	coordinate for the profile, normal to the chord
iasizep	pixel	1x1	size of the squared interrogation area

Table 11: The second way of data, on tensor form (42x42x7).

Page	1st	2nd	3rd	4th	5th	6th	7th
quantity	1st col. xv, 2nd col. yv, the rest NaN	umean	vmean	urms	vrms	$\chi$	okn
units	[-]	[m/s]	[m/s]	[m/s]	[m/s]		

Table 12: The third way on ASCII-format, as an array (42x254) with increasing xv as rows and increasing yv as columns.

Columns	1	2	(3:44)	(45:86)	(87:128)	(129:170)	(171:212)	(213:254)
quantity	xv	yv	umean	vmean	urms	vrms	$\chi$	okn
units	[-]	[-]	[m/s]	[m/s]	[m/s]	[m/s]		

Table 13: The PIV data files. The reference point was the lower left corner in the image corresponding to the image position, see Figure 14. The angle of attack is specified in column 2. The reference coordinates are given in column 3 and 4 ( x,y), the dynamic pressure in col.5 and number of runs in col. 6. Column 10 gives the laser sheet in span wise position (z) from the test section floor.

PIV-measurements												
acronym	$\alpha$	camera pos.	ref.x-pos. (chord-wise)	ref. y- pos.(normal to the chord) [mm]	q(Pa)	nb. of runs	cyl. lens [mm]	camera lense [mm]	z-pos. h [m]	dt ( $\mu$ s)	pulse/acq u.	(pulse/acq. )/15 [s]
A1	15	A	58.40%	-3.6	1000	178	100	60	0.85	25	20	1.333
A2	15	B	49.40%	-1.2	1000	159	100	60	0.85	25	20	1.333
B1	8	B	49.40%	-1.2	1000	270	100	60	0.85	60	25	1.667
C1	8	B	49.40%	-1.2	1000	513	100	60	0.85	60	4	0.267
C2	15	B	49.40%	-1.2	500	725	100	60	0.85	60	8	0.533
C3	15	B	49.40%	-1.2	1000	602	100	60	0.85	60	9	0.600
C4	15	B	49.40%	-1.2	1000	677	50	60	0.85	40	9	0.600
C5	5	B	49.40%	-1.2	1000	810	50	60	0.85	40	9	0.600
E1	15	C	58.42%	12.6	1000	710	100	105	0.85	8	9	0.600
G1	15	D	36.16%	35.8	1000	925	100	105	0.85	5	9	0.600
G2	15	E	15.93%	43.3	1000	691	100	105	0.85	8	9	0.600
G3	15	F	73.49%	0.6	1000	867	100	105	0.85	8	9	0.600
G4	15	G	89.67%	0.9	1000	847	100	105	0.85	8	9	0.600
H1	15	H	32.5%	39.1	1000	1345	50	60	0.55	20	9	0.600
H2	15	I	29%	24.4	1000	680	50	60	0.81	30	4	0.267
I1	15	J	29%	26.8	1000	861	50	60	0.77	40	9	0.600
I2	15	K	29.1%	33.3	1000	890	50	60	0.60	40	9	0.600
I3	0	L	154.2%	-28	1000	546	50	60	0.85	10	9	0.600
I4	5	L	154.2%	-28	1000	970	50	60	0.85	10	9	0.600
I5	8	L	154.2%	-28	1000	1024	50	60	0.85	10	9	0.600
I6	15	L	154.2%	-28	1000	1061	50	60	0.85	7	9	0.600
J1	0	M	154.2%	-43	1000	1006	50	60	0.85	15	9	0.600
J2	5	M	154.2%	-23	1000	1087	50	60	0.85	15	9	0.600
J3	8	N	85.09%	-3.1	1000	1012	50	105	0.85	15	9	0.600
J4	15	O	28.67%	43.3	1000	1102	50	105	0.85	15	9	0.600
J5	15	O	28.67%	43.3	1000	108	50	105	0.85	15	2	0.133
K1	N/A	O	28.67%	43.3	1000	1392	50	105	0.85	58	9	0.600
K2	N/A	O	28.67%	43.3	1000	1002	50	105	0.85	116	9	0.600
K3	N/A	O	28.67%	43.3	1000	150	50	105	0.85	58	9	0.600
A=99-03-02 A=58.4-107.5% (laserpos)												
B=99-03-03 B=49.3-98.5% (vid ytan,a15)												
C=99-03-04 C=58.4-82.5% 1=50-94%												
D=99-03-05 D=36.2-59.8% 2=50-98%												
E=99-03-06 E=15.9-40.1% 3=56-99%												
F=99-03-07 F=73.5-97.4% 3=hela,c50mm												
G=99-03-08 G=89.7-113.4% 4=hela												
H=99-03-09 H=32.5-64.5%												
I=99-03-10 I=29.0-72.2%												
J=99-03-11 J=27.8-69.0%												
K=99-03-12 K=29.1-63.4%												
L=154.3-188.5%												
M=154.3-188.5%												
N=85.1-101.7%												
O=28.7-46.5%												





Issuing organization  Flygtekniska Försöksanstalten Box 11921 S - 161 11 Bromma Sweden	Document no.  FFA 1999-52		
	Date August 1999	Security Unclassified	
	Reg. No. 947/98-23 550/99-23	No. of pages 82	
Sponsoring agency Swedish National Energy Administration	Project no. VU0316	Order/Contract STEM P11550-1 P11550-2	
Title A PIV Study of Separated Flow around a 2-D Airfoil at High Angles of Attack in a Low Speed Wind Tunnel			
Author  Richard Holm and Jonas Gustavsson			
Checked by  Anders Björk	Approved by  Sven-Erik Thor		
Abstract <p>Wind tunnel tests were carried out in order to acquire experimental data for validation of numerical results from Navier-Stokes calculations (CFD-simulations) on airfoils at high angles of attack. The tests were performed on the 21% thick FFA-W3-211 airfoil geometry, 2-dimensional wind tunnel model with 0.45m chord and 2m span. The purpose of the study was to examine the flow field around the airfoil at 8° and 15° angle of attack, in particular to determine the position of the separation and the recirculating region. The wind tunnel tests were carried out at Re=1.25 million. The used measurement techniques were pressure measurement, oil flow visualisation and PIV (Particle Image Velocimetry)</p> <p>The boundary layer transition was triggered at a fixed position (<math>x/c=0.026</math> on the suction side and <math>x/c=0.312</math> on the pressure side) by means of an adhesive zigzag tape. The uncertainties regarding the position of transition was thereby reduced</p> <p>Based on the velocity vector field obtained by the PIV data the velocity profile, boundary layer quantities and the back-flow coefficient were derived. The back-flow coefficient was then used as a criterion for separation</p> <p>The conclusions of the study were:</p> <ul style="list-style-type: none"> <li>• The flow field was determined by PIV and available for comparison with CFD-results.</li> <li>• Based on the velocity field the separation positions, the velocity profile at different chordwise position and boundary layer quantities were derived.</li> <li>• The separation position, for 15° angle of attack, was determined in the PIV measurements to <math>x/c=0.39\pm0.03</math> and in the pressure measurements to <math>x/c=0.40\pm0.05</math> and somewhat subjectively in the oil flow to <math>x/c\approx0.42</math>.</li> </ul> <p>The data are available on file format for comparison with CFD results</p>			
Keywords/Nyckelord aerodynamics, aerodynamic stalling, wind tunnel test, wind energy, 2-D airfoil, separated flow, PIV, velocity field			
Distribution	STEM	VKK-rådet	FFA
Copy no.	1-7	8-17	18-60